Journal of Sound and Vibration 626 (2026) 119656

Contents lists available at ScienceDirect

Journal of Sound and Vibration

journal homepage: www.elsevier.com/locate/jsvi

Serration manufacturing effects on propeller trailing edge noise mechanisms

Jorge Santamaria [a], Sylvain Belliot [b], Marlène Sanjosé [a,*], Romain Gojon [b], Stéphane Moreau [c]

[a] Department of Aerospace Engineering, École de Technologie Supérieure, 1100 rue Notre Dame Ouest, Montréal, H3C1K3, QC, Canada
[b] ISAE-SUPAERO, 10 avenue Edouard Belin, Toulouse, 31400, France
[c] Department of Mechanical Engineering, Université de Sherbrooke, 2500 blvd de l'Université, Sherbrooke, J1K2R1, QC, Canada

ARTICLE INFO

Keywords:
Propeller
Trailing-edge noise
Serration
Manufacturing

ABSTRACT

Trailing edge noise is an important broadband noise source of hovering UAV rotors, which can be reduced by trailing edge serrations. Ayton's theoretical model provides predictions for serrated trailing edge noise generated by a fully turbulent flow over an infinitesimally thin plane. This study assesses the validity of these assumptions by considering the effects of serration installation and manufacturing. Several propellers of the same design were 3D printed and tested in an anechoic room, where far-field noise and aerodynamic performances were collected. The baseline configuration exhibits clear evidence of laminar boundary-layer instability noise. Cut-in and add-on serrations alleviate this noise mechanism. Similarly, to overcome the influence of laminar to turbulent transition over the blade surface, some propellers also include additional tripping elements to trigger the turbulence. Cut-in serrations experience additional vortex-shedding noise characterized by a Strouhal number based on the serration root thickness. The results show that serrations are a viable method to control trailing edge noise at low RPM, where broadband noise dominates over tonal noise. Finally, the analytical predictions successfully capture the noise reduction trends for the add-on serrations. In particular, the model can capture their frequency range of effectiveness and the relative variation of the mitigation with rotational speed. There is better agreement between the model and the experiments for the design that includes tripping. This outcome highlights the importance of considering the manufacturing method during the design phase.

1. Introduction

The widespread use of Unmanned Aerial Vehicles (UAVs), particularly quadcopters commonly referred to as drones, has prompted the aeroacoustic community to focus on the acoustic emissions of these vehicles [1–4], as public acceptance is expected to be a significant barrier to further growth. With increasing numbers of drones flying at low altitudes in populated areas, the propeller noise signature has become a design driver rather than an afterthought.

The scattering of turbulent eddies at the Trailing Edge (TE) of rotor blades can become the dominant broadband noise source in UAVs and in their larger counterparts, Urban Air Mobility (UAM) vehicles, particularly while hovering [5–7]. Several passive noise control methods have been proposed to mitigate Trailing Edge Noise (TEN) by modifying the trailing edge geometry. These methods

* Corresponding author.
E-mail address: marlene.sanjose@etsmtl.ca (M. Sanjosé).

https://doi.org/10.1016/j.jsv.2026.119656
Received 30 May 2025; Received in revised form 29 December 2025; Accepted 7 January 2026
Available online 10 January 2026

Nomenclature

E_n	Modal expansion coefficients for serrated airfoil strip model
FM	propeller Figure of Merit
$2h$	serration amplitude, m
$\beta^2 = 1 - M^2$	compressibility factor
γ	azimuthal angle on the rotor plane, rad
Λ	input to the modal expansion coefficients
λ	serration wavelength, m
Ω	propeller angular velocity, rad s^{-1}
ω	angular frequency, s^{-1}
ϕ_{pp}	wall-pressure fluctuations PSD, $Pa^2 \cdot s$
Π_0	streamwise-integrated wavenumber spectra of wall-pressure fluctuations, $Pa^2 \cdot s/m$
Θ	observer angle in the blade strip frame of reference, rad
θ	observer angle in the rotor frame of reference (elevation from the rotor plane), rad
$\vec{X} = [X, Y, Z]$	observer coordinates in the rotor frame of reference
$\vec{x} = [x, y, z]$	observer coordinates in the blade strip frame of reference
c_Q	torque coefficient
c_T	thrust coefficient
k	acoustic wavenumber, m^{-1}
k_x	streamwise aerodynamic wavenumber, m^{-1}
k_y	spanwise aerodynamic wavenumber, m^{-1}
L	airfoil or blade strip span, m
l_y	spanwise correlation length, m
L_{fl}	aeroacoustic feed-back loop length, m
Q	propeller torque, N.m
R	propeller radius, m
S_0	corrected distance for convection effects, m
S_{pp}	far-field acoustic pressure PSD, dB/Hz
T	propeller thrust, N
U	free-stream velocity, m/s
U_c	convection velocity, m/s

include porous extensions [8,9], trailing edge serrations [10,11], or poro-serrated edges [12]. For small-scale propellers, where rapid prototyping is a viable manufacturing method, there is renewed interest in using serrations to reduce TEN.

While several studies focused on airfoil TEN control with serrations [13], only a handful of investigations examined small propeller TEN reduction. A serration is typically characterized by its amplitude, $2h$, its wavelength λ, and the ratio of these two variables. It has been experimentally demonstrated that sharper serrations, that is $2h/\lambda > 1$, offer better noise reductions [14–17]. This is also consistent with the theoretical findings of Howe [18]. The noise reductions occur at high frequencies and range from 2 to 6 dB, and have been measured for all elevation angles with respect to the rotational plane [16,17]. In addition, it has been found that serrations can reduce broadband noise at hover and forward flight conditions [14–17].

The serration manufacturing method is a crucial factor impacting the propeller acoustic and aerodynamic performance. Serrations can be designed by adding material at the trailing edge as an appendix or by directly carving them into the blade. The former are commonly referred to as add-on serrations, while the latter are referred to as cut-in serrations. Yang et al. [15] found that add-on serrations increase thrust compared to cut-in serrations and ascribed this difference to the increase in blade area. The same authors concluded that serrations along half the blade span yield the same noise reduction as serrations along the full span.

Computational aeroacoustic (CAA) simulations can provide valuable insights into trailing-edge noise generation and mitigation. For airfoil applications, both direct [19] and hybrid acoustic approaches can be used. In the latter, noise source generation and acoustic propagation are resolved in two coupled steps. In the hybrid approach, the far-field sound pressure can be computed using an integral formulation, an acoustic analogy [20–22] assuming free field propagation in most cases or using tailored Green's function [23,24]. Another way involves solving the acoustic field using linearized or non-linearized Euler equations [25–27], accurately accounting for acoustic propagation with diffraction in complex geometries [28,29]. Direct CAA simulations are prohibitively expensive and are currently limited to academic configurations. In contrast, hybrid CAA can be applied for rotor configurations [30,31]. However, the cost of scale-resolving simulations is still too high for rapid design exploration in propellers. Therefore, in the early design phases, hybrid approaches that leverage Reynolds-Averaged Navier-Stokes (RANS) simulations to reconstruct the noise source are an attractive option [13,32,33]. In this category, two main approaches are identified [33]. On the one hand, methods that attempt a stochastic reconstruction of the resolved field [32], and on the other, methods involving only a statistical description of the noise source, the latter being the most computationally efficient approach. Further computational savings can be achieved by using analytical methods where the free-field propagation around an airfoil is computed by means of a half-plane Green's function [34]. Such low-order

methods can be transferred from airfoils to propellers by using strip-based methodologies, such as in Schlinker and Amiet [35], to obtain a fully analytical formulation for trailing edge noise prediction.

Given the large number of serration shapes, sizes, and possible configurations, UAV designers can benefit from low-order methods based on analytical TEN models, particularly during early design phases. The noise source modeling begins with the propeller aerodynamics and boundary-layer parameters calculation near the trailing edge using RANS simulations to properly account for the blade loading and the three-dimensional flow on the blade. Having obtained the boundary-layer characteristics, several approaches [13,36,37] are available to reconstruct the turbulent wall pressure spectra required by trailing-edge noise models. The TNO-Blake model uses information on the mean shear profile and the vertical velocity spectrum to calculate the wall-pressure spectrum and requires the approximation of a multiple integral [13]. Therefore, it might not be ideal for fast calculations. A quicker alternative uses a semi-empirical approach where the one-point wall-pressure spectrum is modeled based on a universal spectrum shape, requiring only local characterization of the boundary layer [38]. The latter approach was successfully applied by Sanjosé and Moreau [39] for an engine cooling fan, by Lallier-Daniels et al. [40] for a large propeller, and by Santamaria et al. [41] for a small propeller.

Having modeled the noise source, i.e., the wall-pressure fluctuations spectrum, an analytical model is used to obtain the propeller far-field acoustics by considering several blade strips along the radial direction. Several theories have been developed for the acoustic scattering of disturbances by a half-plane edge [34,42,43]. Because of its simplicity, Amiet's model has been used extensively to predict airfoil [13] and propeller trailing edge noise [44]. For serrated edges, Lyu's model [45], based on Amiet's model, gives accurate results at the cost of lengthy computations and requires a truncation of the solution to a second-order expansion. Akila et al. [46] used Lyu's model in combination with Schlinker and Amiet's model [35] to predict noise reductions from a serrated propeller, finding a fair agreement in the noise reduction trends for the first-order solution when compared to Lattice Boltzmann (LBM) simulations. An alternative approach based on the Wiener-Hopf method was proposed by Ayton [47] and later simplified for rapid calculations [48]. The latter model was then heuristically modified to use it in rotors by Li and Lee [49]. Applying this model, Santamaria et al. [41] showed that the square wave serration might be better suited for low Reynolds number propellers and that using different serration shapes along the span gives better noise reductions at specific frequencies compared to using single shapes. Despite growing interest in using serrations for passive TEN control of UAV/UAM rotors, few studies have addressed the effects of serration manufacturing and installation, i.e., how serrations are added to the propeller. Additionally, all trailing edge noise models for both straight and serrated edges treat the blade strips as infinitesimally thin plates and assume fully turbulent boundary layers. Therefore, the validation of analytical models requires more experimental data to establish their capabilities and limitations.

This work focuses on the manufacturing effects of trailing edge serrations tested experimentally and on the comparison of measured noise reductions with theoretical predictions for a representative drone propeller in hover. Section 2 summarizes the methodology together with the analytical models. Section 3 then presents the propeller serrations design and manufacturing based on the theoretical noise reductions. Section 4 details the measurement techniques and post-processing of the acoustic signals, while Section 5 discusses the broadband noise sources for the baseline propellers and the influence of tripping. Lastly, in Section 6, the aerodynamics and acoustics results from the experimental measurements on serrated propellers are discussed and compared with the theoretical noise reductions.

2. Analytical prediction of propeller trailing edge noise

This section presents a low-order methodology for calculating propeller TEN based on analytical models for straight and serrated edges, using Schlinker and Amiet [35] model with a strip theory approach. The method requires modeling the wall-pressure spectrum close to the trailing edge using semi-empirical models. The methodology is implemented in the in-house code PyFanNoise to compute the propellers far-field acoustics, and is briefly summarized next.

2.1. Propeller trailing edge noise

The calculations use a strip-theory-based method [35] to calculate rotor TEN. The method assumes that the noise from the individual blades is uncorrelated and that the frequency of the fluctuations is much larger than the rotor rotational frequency. The model also requires several matrix transformations to account for the blade geometry and to convert between the strip coordinates ($\vec{x} = [x, y, z]$) and the rotor coordinates ($\vec{X} = [X, Y, Z]$). Sinayoko et al. [50] compared Schlinker and Amiet's method with the exact Ffowcs Williams and Hawkings' solution in the frequency domain that takes into account the acceleration effects of the source, and found perfect agreement. The far-field TEN of the rotor is calculated by a weighted average of the strip acoustic pressure over one rotor revolution. The weighting function accounts for the Doppler shift through the emission frequency $\omega'(\gamma)$. Thus, the far-field acoustic pressure spectrum from the rotor is given by:

$$S_{pp}^{\text{rotor}}(\vec{X}, \omega) = \sum_{\text{strips}} \frac{B}{2\pi} \int_0^{2\pi} \left(\frac{\omega'(\gamma)}{\omega} \right)^2 S_{pp}^{\text{strip}}\left(\vec{x}, \omega'(\gamma)\right) d\gamma \tag{1}$$

with B the number of blades. The integration variable γ sweeps the angular shift of the observers over a whole revolution ($0 \leq \gamma \leq 2\pi$). The full-blade rotor noise is obtained by adding the contribution from all blade segments.

The acoustic power for an isolated rotor is obtained by the integration of the noise levels over a sphere, the center of which matches the rotor center. The sphere is discretized by a set of observers uniformly distributed along the longitude and latitude directions on the sphere. The sound power level (SWL) in dB can be calculated from the acoustic power in Watt for a resolution of $\Delta f = 1$ Hz and a reference power of 10^{-12} W.

Once geometry and flow parameters have been defined in PyFanNoise, the SWL prediction for one propeller can be obtained in less than a minute providing a suitable method for design space exploration. This low return time is obtained thanks to the fully-analytical models that are used to compute the blade strip response derived for semi-infinite flat plate.

2.2. Blade strip trailing edge noise

The TEN calculation for each strip uses Li and Lee [49] extension of the rapid Lyu and Ayton's model [48]. The latter model uses the Wiener-Hopf technique to find an analytical solution to the convected Helmholtz equation on a semi-infinite plane with a serrated trailing edge of amplitude $2h$ and wavelength λ. Although the use of the Wiener-Hopf method gives the pressure field in the whole domain, it requires the approximation of an inverse Fourier transform with the method of stationary phase to obtain a closed solution. This approximation limits the model to cylindrical, two-dimensional noise radiation and infinite span. Moreover, no back-scattering solution has yet been derived, which limits the solution to high frequencies. Li and Lee's main modifications consist of the inclusion of finite span, matching spherical propagation of acoustic waves, and the addition of spanwise observer coordinates. The model is given by:

$$S_{pp}^{\text{strip},LL}(\vec{x},\omega) \approx \frac{L\bar{k}\beta^2}{4\pi^2 S_0^2}\frac{\chi+\bar{k}}{(\chi-\bar{k}\cos\Theta)^2}\sin^2\left(\frac{\Theta}{2}\right)\sum_{n=-\infty}^{+\infty}|E_n(\Lambda)|^2\,\Pi_0\left(\frac{\omega}{U_c},k\frac{y}{S_0}\right) \tag{2}$$

where L is the airfoil or blade strip span with $\bar{k}=k\beta$, $\chi=k_x\beta+kM/\beta$ the compressibility corrected acoustic and streamwise wavenumber respectively, and Θ the angle between the x-axis and the observer in the blade strip coordinate system.

The modal expansion coefficients $E_n(\Lambda)$ where $\Lambda=(\chi-\bar{k}\cos(\Theta))2h/\beta$ regulate the degree of interference for each trailing edge geometry with the zeroth-mode dominating while the remaining modes become important when $k\lambda/\beta > 2\pi n$. Ayton and Chaitanya [51] provided expressions for the modal expansion coefficients of different geometric shapes. In this study, 20 modes are used for the calculation based on previous tests [41,52].

As pointed out by Tian and Lyu [53], the extension of the simplified Ayton's model for rotating blades is not straightforward, given the assumptions made in its derivation. However, Li and Lee showed that some trends are accurately predicted with their proposed extension. Additionally, Ayton's model simplicity and fast computational time make it attractive for earlier design phases and/or optimization algorithms. These are the reasons why the model was chosen in this study.

2.3. Wall-pressure wavenumber spectrum

The fundamental input to the strip analytical model of the previous section is the wavenumber-frequency spectrum of wall-pressure fluctuations (Π_0). For fully-turbulent boundary layers, the latter term can be simplified to the product of the local spectrum (ϕ_{pp}) and the spanwise correlation (l_y) length [54]:

$$\Pi_0\left(\frac{\omega}{U_c},k\frac{y}{S_0}\right)=\frac{1}{\pi}\Phi_{pp}(\omega)\,l_y\left(\omega,k\frac{y}{S_0}\right) \tag{3}$$

where U_c is the convection velocity of eddies, here assumed to be 70% of the boundary layer edge velocity. Note, however, that this velocity is most likely varying along the blade span according to different local adverse pressure conditions [55] Corcos' model is classically used to compute the spanwise correlation length for turbulent boundary layers:

$$l_y(\omega,k_y)=\frac{\omega/(b_cU_c)}{k_y^2+\omega^2/(b_cU_c)^2}, \tag{4}$$

where k_y is the aerodynamic spanwise wavenumber, and b_c is the inverse of the exponential decay of the spanwise correlation length, and it is assumed to be 1.47 [39].

For modeling the wall-pressure fluctuation spectrum, several models are available [38]. This study uses Lee's [38] model. The model inputs are extracted following the methodology given in [39].

3. Serrations design and propeller manufacturing

3.1. Design of serrations with the RANS-based approach

Using the methodology and models presented in section II, Santamaria et al. [41] showed that it is possible to predict broadband noise of small propellers with reasonable accuracy for straight edge. The predictions using Amiet's model were within about 3 dB of the measurements in the 1–10 kHz frequency range. Moreover, Li and Lee's extension of Ayton's model matches Amiet's model for frequencies above 4 kHz in the limit of zero serration amplitude. In their study, the RANS simulations mimic the experimental setup from Gojon et al. [56] for a 2-bladed, constant 10° pitch, 2.5 cm in chord, 25 cm in diameter rotor with a NACA 0012 cross-section, for which both experimental and high-fidelity numerical data are available [57].

The RANS simulations [41] were performed for the operational range between 4000 and 8000 RPM, and two turbulence models were compared: the fully turbulent k-ω SST, and its transitional version using the local-correlation-based γ-Re_θ model. The simulations were validated with experimental data, with the thrust coefficient and figure of merit falling within the 95% confidence interval for

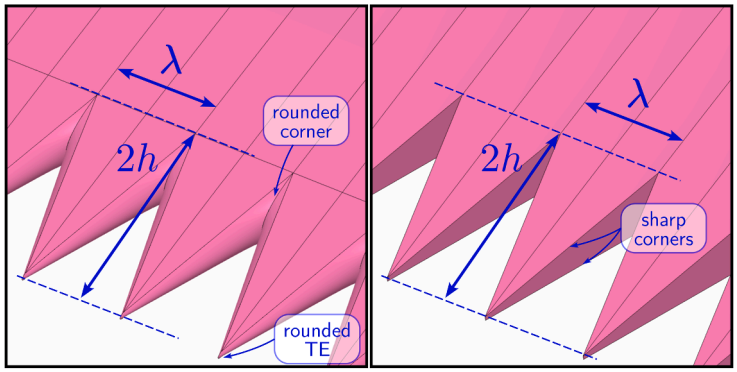

Fig. 1. Smooth (left) and sharp (right) teeth for propellers with cut-in serrations.

Table 1
Test matrix with designation.

		Clean	Tripped (T)	Designation
Baseline	Straight edge	x	x	B-(T)
	Flat plate add-on	x	x	BP-(T)
Cut-in	Sharp	x		C-SH
	Smooth	x		C-SM
Add-on	Sharp	x	x	A-ST-(T)

both cases. The flow parameters required by the analytical approach were extracted at 50 points along the span and at 85% of the chord, following Sanjosé and Moreau [39].

Using the fully turbulent results, the serration dimensions were chosen based on the extraction of boundary-layer parameters close to the trailing edge, particularly the boundary-layer thickness close to the tip (δ_{tip}). The serration amplitude and wavelength were set to $2h = 2\delta_{\text{tip}} = 5$ mm and $\lambda = h$ following the recommendations in [10,13] and [58,59] respectively.

3.2. Serrated propeller geometries

Having defined the serration parameters, several strategies may be used for their installation, yielding several CAD models of serrated propellers. The serration types are divided into three categories: add-on (A), cut-in sharp (C-SH), and cut-in smooth (C-SM). The first case is a flat plate appendix where the serration patterns are carved. The division between sharp and smooth serrations for the cut-in case is necessary since blunt edges could result in vortex-shedding noise [11] and must be considered at early design stages. Note that the smooth teeth in the case of a serrated controlled-diffusion (CD) airfoil were shown to add no extra noise sources and provided very similar aerodynamic performances compared to the straight edge [52,60]. The detail of sharp and smooth teeth is shown in Fig. 1. Note that to make a fair comparison, two baseline propellers are proposed. The original propeller (B) without any modification will serve as the baseline for the propellers with cut-in serrations, whereas a modified propeller with a flat plate add-on (BP) will be used to assess the add-on serrations.

The thickness at the trailing edge was the main manufacturing constraint and was initially set at a minimum of 0.1 mm. For propellers with cut-in serrations, the teeth are thicker at the root (≈ 1.4 mm), and the minimum thickness can be obtained at the tip. For the add-on cases, the tapered NACA 0012 profile end is replaced with a flat plate of constant thickness and sufficient length to allow for serration printing. The flat plate thickness was set to 0.4 mm, as lower values resulted in loss and/or detachment of teeth during printing. The resulting mean chords are the same as the baseline for the propellers with cut-in serrations, whereas they are slightly larger for the add-on ones.

Additionally, given the fully turbulent assumption of the analytical models, the propellers with add-on serrations were manufactured in two configurations: a "clean" one and one with tripping cylinders at 10% of the chord. Following the design by Gowree et al. [61] on a similar, albeit 3-bladed, NACA 0012 propeller, the tripping height and diameter were set to 140 μm and 1.37 mm respectively, with a distance between cylinders of 2.54 mm. The complete test matrix and some of the blade planforms are shown in Table 1 and in Fig. 2, respectively.

3.3. Propeller manufacturing

The propellers are manufactured using stereolithography (SLA) with the Form-3L 3D printer using the Formlabs RIGID 4000 resin. Several experimental campaigns [56,61,62] required manufacturing similar propellers and helped validate this process. SLA-printed objects are continuous and highly isotropic and enable the creation of parts with smooth surface finishes and fine features. The precision is on the order of 0.1 to 0.3 mm for fine features and within 0.5% for larger dimensions.

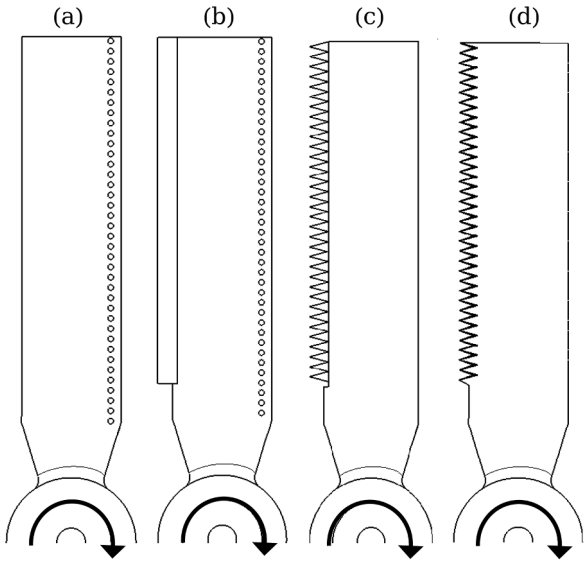

Fig. 2. Planforms of some tested propellers: (a) straight-edge with trip (B-T), (b) add-on flat plate with trip (BP-T), (c) add-on serration (A-ST), and (d) cut-in smooth serration (C-SM).

Fig. 3. 3D printed propeller with Sawtooth cut-in sharp serrations (C-SH).

As serrations are rather thin appendages (0.4 mm) and relatively long (5 mm), their manufacturing is challenging. The automatic algorithms of the printing software define the layout, orientation, and support of the print, but it yields excessive support on the serrations. Therefore, the support distribution was manually modified, by seeking a balance between supporting the part and placing supports on fragile parts. Finally, with a layer thickness of 0.1 mm, the estimated printing time is around 20 hours for 4 propellers.

After the printing, the rotors are washed with isopropyl alcohol to remove any resin remaining on the rotor surface. Then, they are UV-treated to finalize the polymerization process and improve part strength. The support structures required for the printing process are cut out, then the part is hand-sanded, as it has been shown by Gowree et al. [61] that surface roughness can impact rotor aerodynamics and acoustics. During this final stage, static balancing is also carried out.

Fig. 3 shows the propeller with cut-in sharp serrations (C-SH). Fig. 4 shows the propeller with an add-on plate (BP) during static balancing.

4. Experimental set-up and signal processing

4.1. Measurements

The propellers designed in the previous section were tested in the ISAE-SUPAERO anechoic room. This facility is acoustically treated in the 80 to 16 000 Hz frequency range and has dimensions of 5.02 m long, 5.24 m wide, and 5.34 m high from wedge-tip to wedge-tip. A Faulhaber 3274G024BP4 3692 electric brushless motor, which emits less noise than conventional off-the-shelf motors, drives the isolated rotors positioned in the center of the chamber. A six-axis ATI (Apex, NC) Nano17 load cell records thrust and torque, while a directivity antenna comprising 13, 1/4" GRAS microphones, measures far-field noise. The microphones are placed

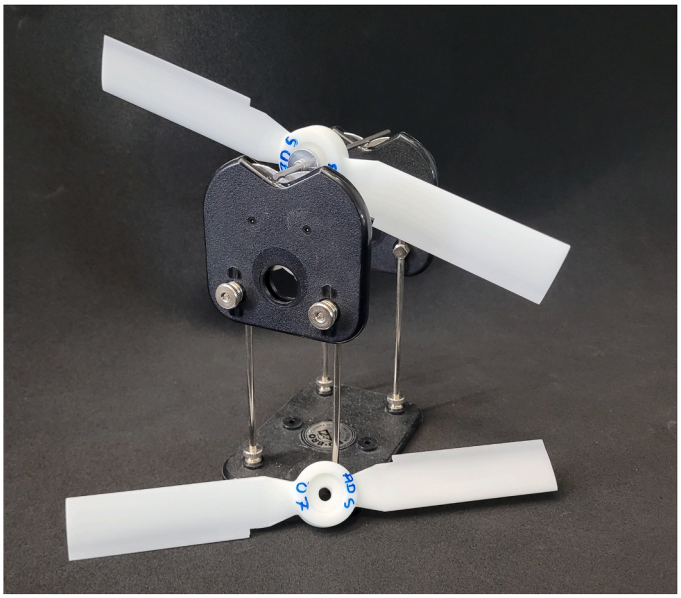

Fig. 4. 3D printed propeller with flat plate add-on (BP) during static balancing.

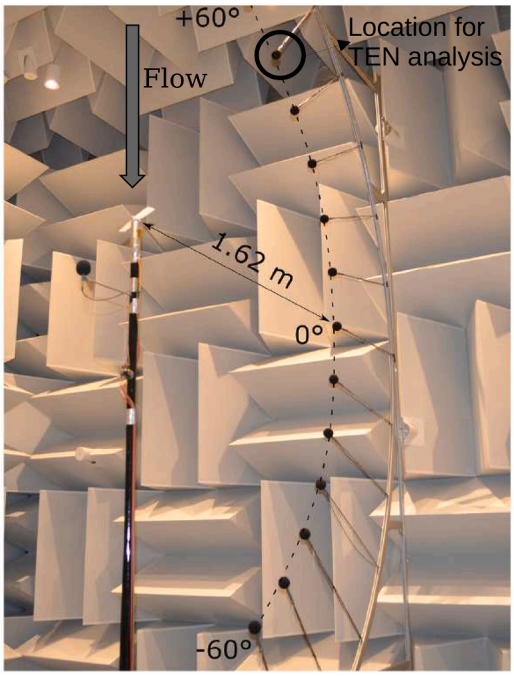

Fig. 5. Experimental set-up with the baseline propeller.

at a distance of 1.62 m from the rotor center and spaced every 10° from −60° to 60° with the rotor plane at 0° as shown in Fig. 5. Note that recirculation was assessed during the first experimental campaign with the 3D-printed NACA 0012 propellers in [56]. Using spectrograms, they showed that recirculation effects were minimal for thrust up to 3.73 N. All the results presented in this study are within that threshold.

Acoustic data are acquired at a sampling frequency of 51.2 kHz for 16 s. Acoustic narrowband spectra are obtained from time signals using Welch's periodogram method with a Hanning window applied on 50 segments, using a 50% overlap and an amplitude correction factor. The frequency resolution is $\Delta f = 3.125$ Hz. Following Zawodny and Boyd [63] the random SPL uncertainty is ± 0.45 dB.

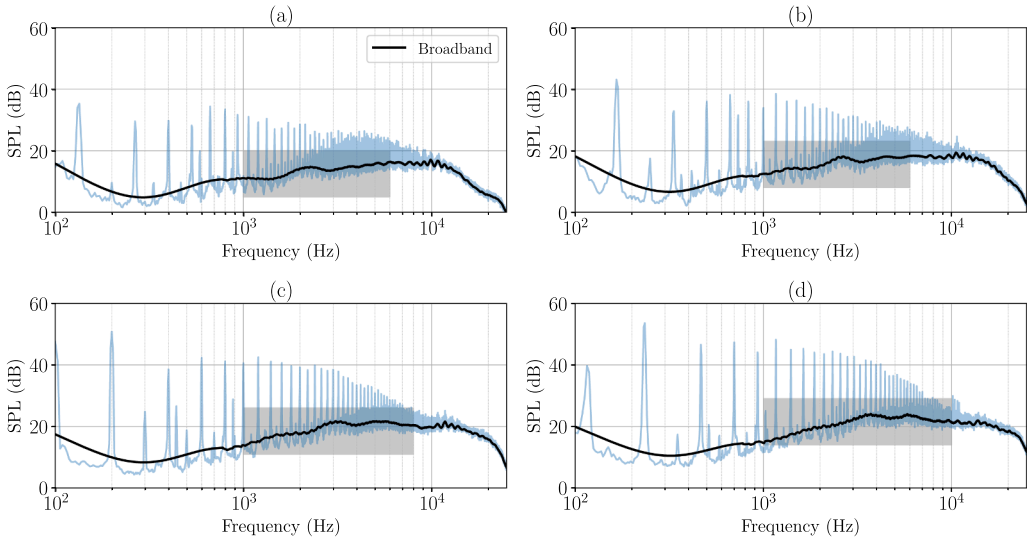

Fig. 6. SPL and extracted broadband signal at 60° from the rotor plane for straight edge propeller at (a) 4000 RPM, (b) 5000 RPM, (c) 6000 RPM, and (d) 7000 RPM. The gray zones correspond to trailing edge noise from the turbulent boundary layer scattering.

4.2. Signal processing

Following the measurements, time-averaged thrust, torque, and power results were calculated and are presented in a dimensionless form for the thrust coefficient C_T and the Figure of Merit FM, which is the ratio of ideal power to actual power, given in Eqs. (5) and (6).

$$C_T = \frac{T}{\rho \pi R^2 (\Omega R)^2} \tag{5}$$

$$FM = \frac{T^{3/2}}{\Omega Q \sqrt{2\rho\pi R^2}} \tag{6}$$

For the acoustic results, the broadband component of the spectrum is necessary to assess the serration effect. The broadband component is obtained using a Savitzky-Golay filter [64], as implemented in the open-source signal processing library SciPy. The filter requires two parameters: the window length and the polynomial order. Tuning these two parameters results in filtering out the shaft and BPF harmonics, leaving the broadband signal. In the present work, the Savitzky-Golay filter is applied with a window spanning 500 samples and a polynomial order of 6. The broadband noise (BBN) levels are calculated by integration of the filtered signal between 1–16 kHz. In addition, the acoustic signals of each propeller are also characterized by peak in the raw spectra at the blade passing frequency (BPF) and the overall sound pressure levels (OASPL). The OASPL is computed by integration of the raw spectra between 80–16 000 Hz following [56,61].

5. Evaluation of baseline geometries

First, the noise generated by the straight-edge propeller at different RPMs is analyzed. Classical scaling laws for airfoil are used in the context of a low-speed propeller to identify noise generation mechanisms. Next, the effects of the add-on plate and the tripping cylinders on the baseline are discussed.

5.1. Identification of noise sources for the baseline propeller

The acoustic spectra of the straight-edge propeller is shown in Fig. 6 for different RPMs. The broadband signal shown in black in Fig. 6 consists of two overlapping humps. The first one is between 1–10 kHz without any clear peaks (highlighted in grey zones), while the second one has several peaks, and their frequency depends on the RPM. When scaled with the fifth power of V_∞, the blade velocity at 75% span (r_{75}), the spectra at all RPM collapsed as shown in Fig. 7. This stresses the non-compact dipole nature of the source, and this hump can be attributed to trailing-edge noise. The second hump, however, does not follow this scaling, as it is the consequence of laminar boundary layer instability tones, as demonstrated next.

The filtered spectra in Figs. 6 and 7 reveal well-defined peaks for most RPMs. A vertical offset is added to the individual spectra to aid visualization of the peaks in Fig. 8(a). The number of peaks and their prominence decrease as the rotational speed increases, demonstrating a Reynolds number dependency. The frequencies of the identified tones are then scaled with the chord-based Reynolds

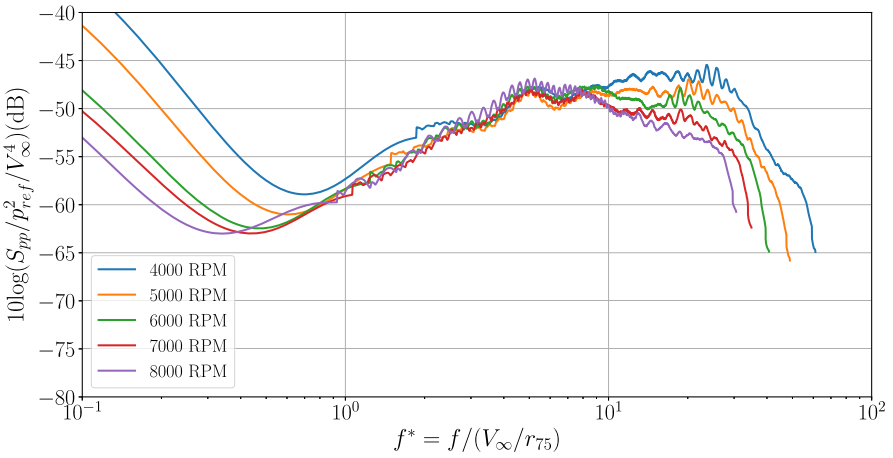

Fig. 7. Scaled baseline extracted broadband spectra as a function of Strouhal number based on V_∞, the blade velocity at 75% span (r_{75}).

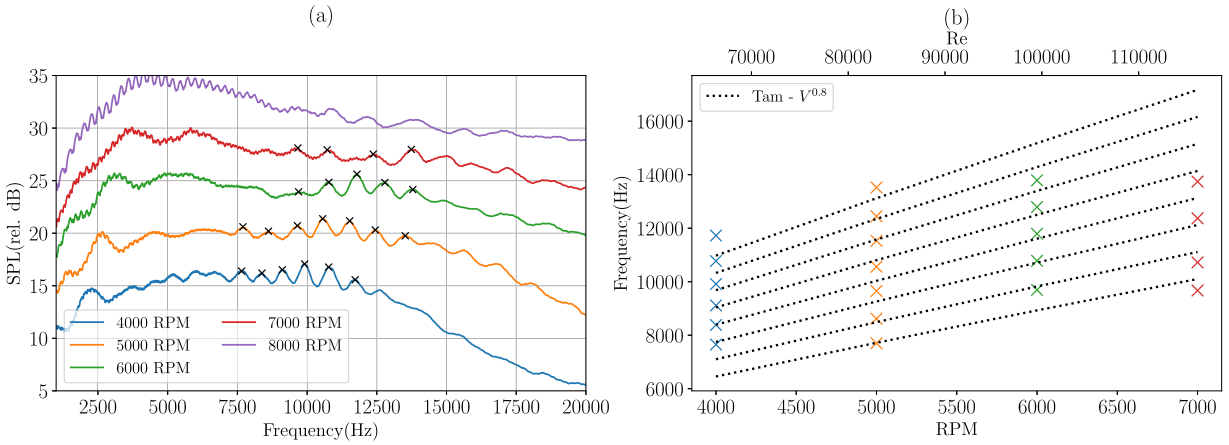

Fig. 8. (a) Filtered spectra and laminar boundary layer tones at different RPM (with arbitrary SPL offset) and (b) tone scaling with Reynolds number.

number (top scale) in Fig. 8(b). The tones follow the well-known ladder-type pattern, and a power fit reveals a dependency of $V_\infty^{0.8}$, in good agreement with the initial findings by Paterson et al. [65] and Tam [66].

The good agreement with the scaling, along with the low Reynolds number, suggests that the tones are the consequence of an aeroacoustic feedback loop between the instabilities in the transitional boundary layer and the acoustic waves radiated from the trailing edge. The frequency between consecutive peaks at each RPM is almost constant and can be used to infer the feedback-loop length, L_{fl}, from the following relationship for the nth tone [67,68]:

$$\frac{f_n\, L_{\text{fl}}}{V_\infty} = \left(n + \frac{1}{2}\right)\left(\frac{1}{a} + \frac{M_\infty}{1 - M_\infty}\right)^{-1} \tag{7}$$

where a, the ratio of the average instability convection speed to V_∞, is fixed to 0.4 [67]. By subtracting the equations between two consecutive tones, the following expression is obtained:

$$\frac{\Delta f\, L_{\text{fl}}}{V_\infty} = \left(\frac{1}{a} + \frac{M_\infty}{1 - M_\infty}\right)^{-1} \tag{8}$$

Using the average distance between peaks in Fig. 8, the feedback-loop length, L_{fl}, is estimated to be 18.5, 19.7, and 22.2 mm for the 4000, 5000, and 6000 RPM cases, respectively. Note that all these values are lower than the propeller chord and increase with the Reynolds number, which suggests that the transition location moves upstream with increasing RPM.

Moreover, Pröbsting et al. [69] identified different regimes of tonal noise on a NACA 0012 airfoil depending on whether the tones come from the suction or pressure side, or both, as shown in Fig. 9. Since the airfoil section of the propellers used in the present study is NACA 0012, an estimate of the effective angle of attack and Reynolds number along the span is required to use the regime chart. The transitional RANS results from Santamaria et al. [41] on the same baseline propeller of this study provide the effective angle of

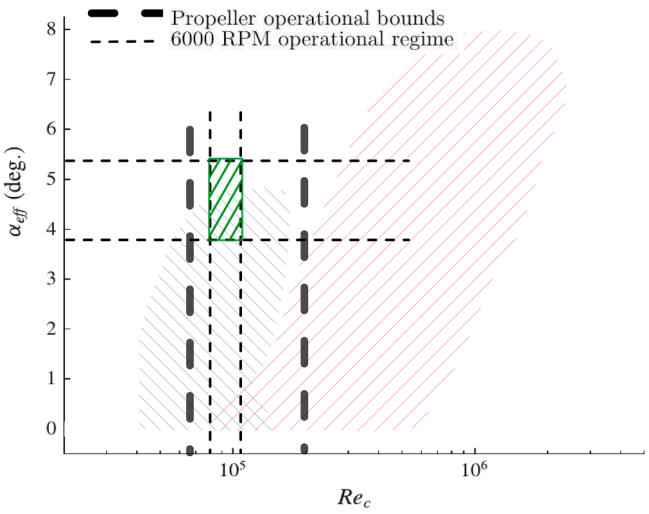

Fig. 9. Regimes of tonal noise generation. Suction (blue, hatched) and pressure (red, hatched) side dominated. (adapted from Pröbsting et al. [69]. Zones of transitional flow in the propeller (green, hatched). (For interpretation of the references to colour in this figure legend, the reader is referred to the web version of this article).

attack and Reynolds number ranges marked in green in Fig. 9. Extraction details and calculation of the effective angle of attack are shown in Appendix A.

The green zone matches the suction-dominated regime, thus adding further evidence that the tones identified in the baseline spectrum come from instabilities in the transitional boundary layer on the suction side. The frequency and levels of this noise source are highly dependent on the manufacturing process [7] as shown in Appendix B for identically designed propellers with different materials and manufacturing methods. Furthermore, as shown later, the filtered spectra for the suction side tripped propeller do not display these tones.

5.2. *Effects of forced transition*

The original baseline propellers (with and without add-on plate) are compared with their tripped counterparts. From an aerodynamics point of view, the presence of the cylinders has two effects: first, they create excrescence drag, and second, they force turbulent flow over the blade. These two effects combined yield lower aerodynamic performance. This is confirmed in Fig. 10, where both the thrust and the figure of merit are lower for the tripped case (B-T) at all RPMs when compared to the baseline (B). This is in good agreement with the original results from Gowree et al. [61]. Interestingly, this trend is not followed for the add-on plate tripped (BP-T) case, which generates the most thrust and has the second-best Figure of Merit from the four baseline propellers. Additionally, it is noted that while the relative difference between the baseline (B) and its tripped twin (B-T) is constant throughout the RPM range, the gap between the clean and tripped baseline with the plate reduces with increasing RPM.

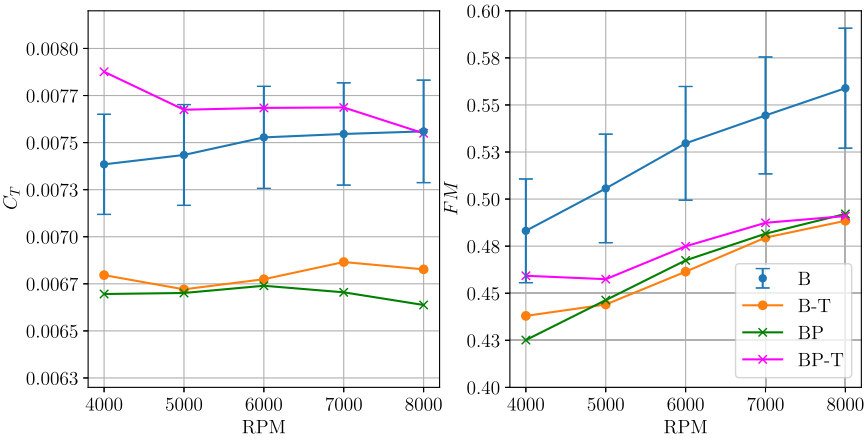

Fig. 10. (a) Thrust coefficient and (b) Figure of Merit for clean and tripped propellers with a straight edge (B, B-T) and add-on plate (BP, BP-T).

The impact of the tripping cylinders on the far-field acoustics is shown in Figs. 11 and 12 for the baseline and the propeller with an add-on flat plate, respectively. For the former, the forced transition is seen to reduce broadband noise, particularly at low RPM. As demonstrated in the previous section, this is due to the elimination of laminar boundary layer instability tones; the same explanation was suggested by Gowree et al. [61]. Note that the presence of a laminar separation bubble (LSB) around mid-chord has also been confirmed recently by high-fidelity simulations [70,71]. At 4000 RPM, the hump associated with this noise source is seen to disappear due to the effect of the trip. At higher RPMs, where natural transition is most likely to occur, the trip still reduces the broadband noise at all frequencies, thus underlying the presence of a possible different noise mechanism.

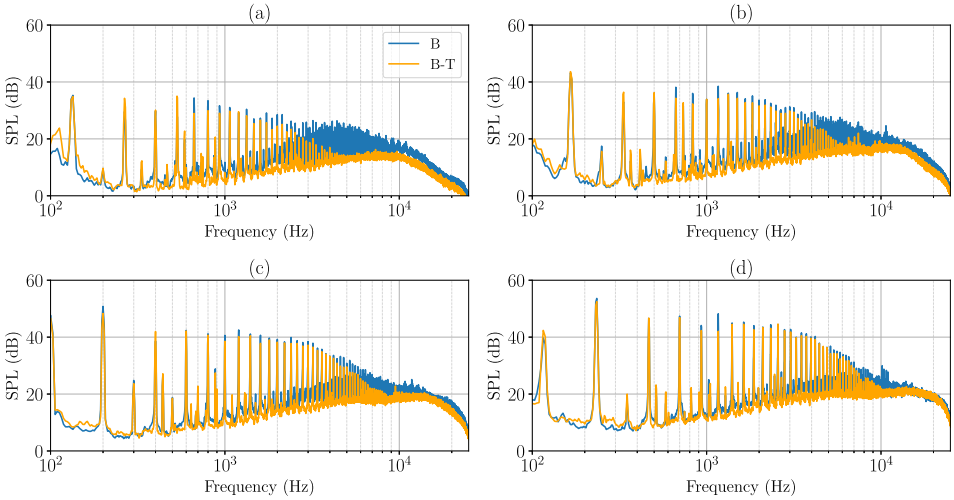

Fig. 11. SPL at 60° from the rotor plane for clean (B) and tripped (B-T) propellers with a straight edge at (a) 4000 RPM, (b) 5000 RPM, (c) 6000 RPM, and (d) 7000 RPM.

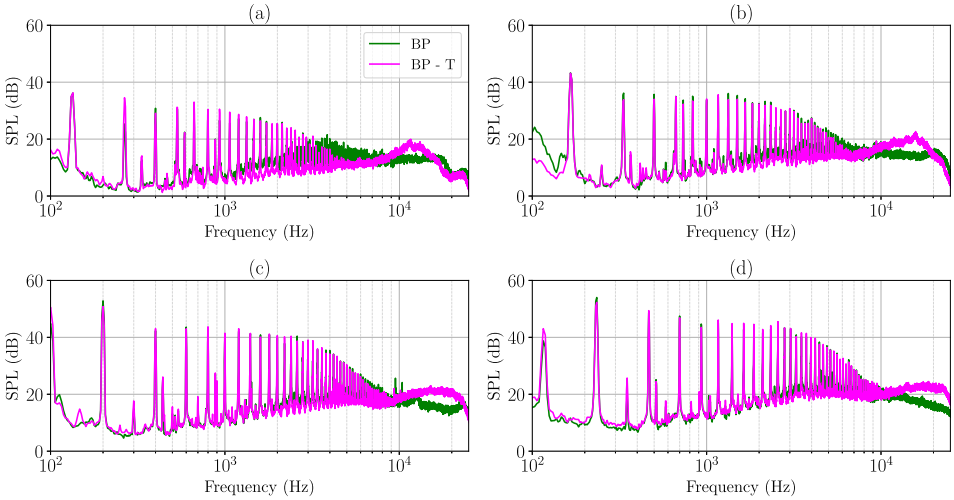

Fig. 12. SPL at 60° from the rotor plane for clean (BP) and tripped (BP-T) propellers with an add-on flat plate at (a) 4000 RPM, (b) 5000 RPM, (c) 6000 RPM, and (d) 7000 RPM.

The spectra for the clean and tripped propeller with the add-on plate show a different behavior. At 4000 RPM, the tripped case reduces broadband noise below 8 kHz, then there is a noise increase between 8–15 kHz due to a hump centered at 12 kHz and a reduction beyond this range. Similar trends are observed at different RPMs. It is hypothesized that the junction modifies the boundary layer and thus its scattering at the plate edge deviates from a fully turbulent boundary layer. Future numerical simulations will investigate such effects in detail.

Directivity patterns for the BPF, broadband noise (BBD), and the overall sound pressure level (OASPL) are shown in Figs. 13 and 14 for the four rotors studied in order to gain more insight on differences in noise emissions. While the forced transition reduces broadband noise, its effect on the BPF is almost negligible for both the baseline and the propeller with the add-on plate. Regarding the

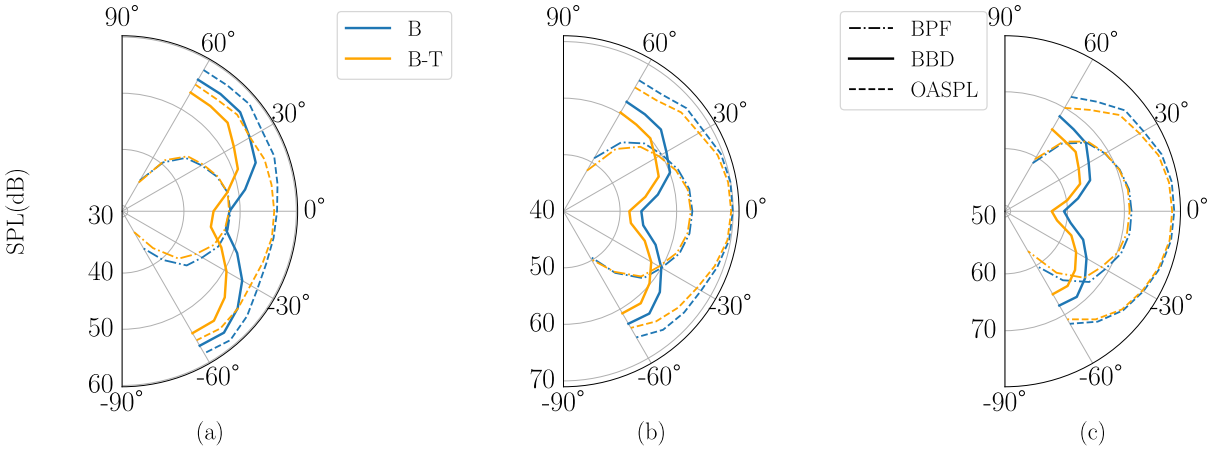

Fig. 13. BPF, Broadband, and OASPL directivity for clean (B) and tripped (B-T) propellers with a straight edge (a) 4000 RPM, (b) 6000 RPM and (c) 8000 RPM.

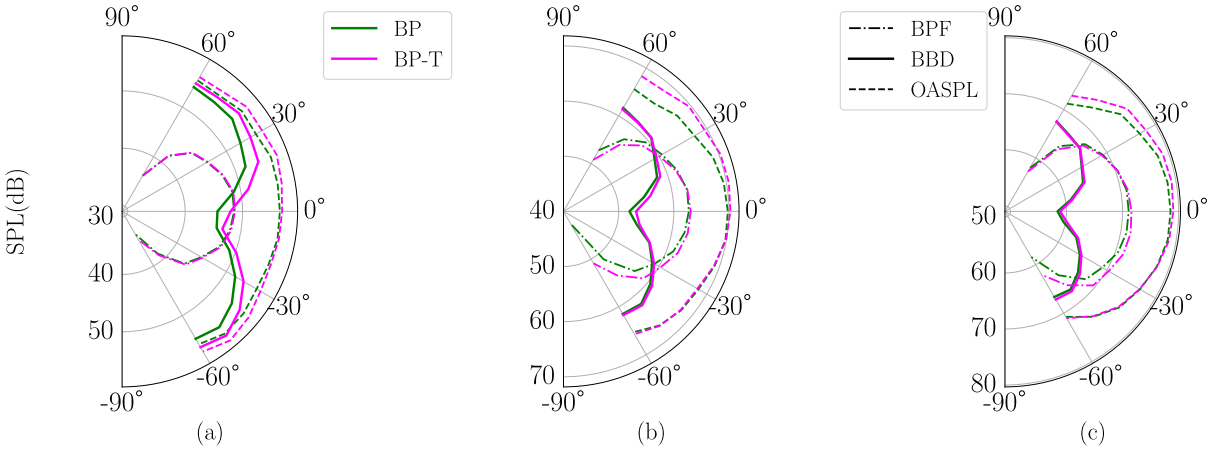

Fig. 14. BPF, Broadband, and OASPL directivity for clean (BP) and tripped (BP-T) propellers with an add-on flat plate at (a) 4000 RPM, (b) 6000 RPM, and (c) 8000 RPM.

OASPL, the tripped baseline (B-T) has the lowest noise levels at 4000 RPM closely followed by the baseline with the add-on plate. The noise reductions from the add-on plate with the trip at lower frequencies are almost outweighed by the aforementioned secondary hump and match the levels of the baseline for observers close to the rotational plane.

6. Evaluation of serrated geometries

The results for the cut-in serrations are presented first, followed by the add-on ones. Then, the effects of the tripping cylinders on the add-on serrated propellers are discussed. Lastly, a comparison with the theoretical noise reductions is made for all cases.

6.1. Cut-in serrations

In this section, the aerodynamics and acoustic effects of cut-in trailing edge serration are discussed. The serrations are either sharp or smooth as summarized in Table 1. To investigate the impact of the 3D printing method, two samples of each serrated rotor have been manufactured and compared here.

Fig. 15 shows the thrust coefficient and the Figure of Merit for straight-edge (B), sharp (C-SH), and smooth (C-SM) cut-in serrated propellers. Two sets of results are shown for the sharp and smooth serrated propellers, corresponding to data obtained for each sample. Volsi et al. [62] performed an uncertainty quantification analysis on the same test stand and on a similar propeller by repeating aerodynamics measurements at the same RPM. Using their measured mean and standard deviations, the aerodynamic loads relative uncertainties were calculated and scaled by the present results for the straight-edge propeller. The results of this linear scaling are presented as error bars corresponding to a confidence interval of 95%.

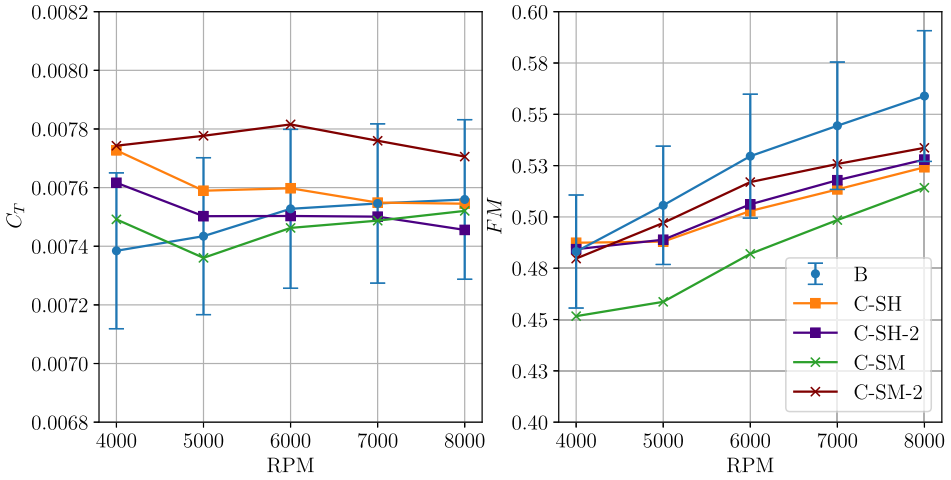

Fig. 15. (a) Thrust coefficient and (b) Figure of Merit for propellers with a straight edge (B), sharp (C-SH), and smooth (C-SM) cut-in serrations.

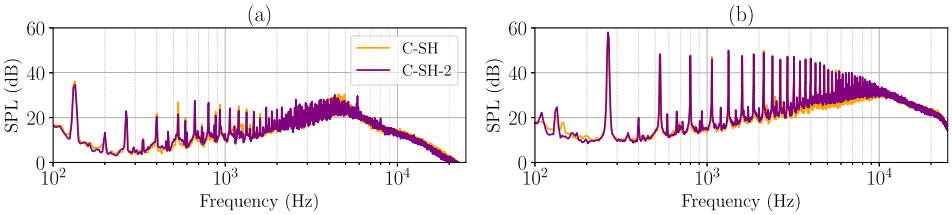

Fig. 16. SPL at 60° from the rotor plane for propellers with sharp cut-in serrations (a) 4000 RPM and (b) 8000 RPM.

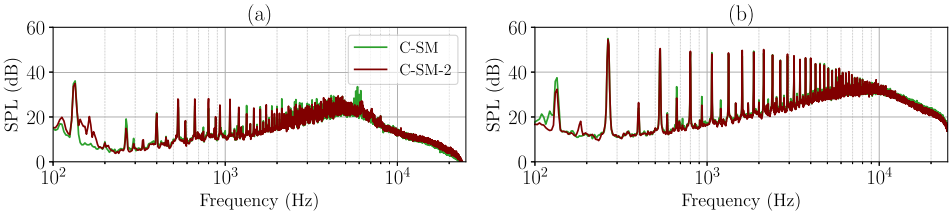

Fig. 17. SPL at 60° from the rotor plane for propellers with smooth cut-in serrations (a) 4000 RPM and (b) 8000 RPM.

In terms of repeatability, the differences between the sharp-teeth propellers are found to be less than the ones between the smooth-teeth ones, with an average relative difference of less than 2% for the former and 4% for the latter. The geometrical complexity of the smooth teeth may explain this trend. Below 6000 RPM, all the serrated propellers are seen to fall within the baseline uncertainty range, except for one of the smooth cases. At the highest RPM, the sharp and smooth cases have a 5% and an 8% decrease in the FM, respectively, for the worst-performing samples. These results highlight the importance of assessing the repeatability of the manufacturing method for serrated propellers, as minor changes in the teeth geometry may give large uncertainties in performance estimates.

To assess the repeatability in terms of acoustics, the spectra at the lowest and highest RPM are shown in Figs. 16 and 17 for the propeller samples with sharp and smooth teeth respectively for an observer at 60° from the rotational plane. Additionally, Table 2 shows the absolute differences in dB between samples for the BPF, the broadband noise (BBD), and the Overall Sound Pressure Level (OASPL) for the same observer position.

Unlike the aerodynamic performances, the relative acoustic differences between samples of the same geometry are less pronounced. At the lowest RPM, the spectra for both sharp- and smooth-teeth propellers show around 1 dB difference at the BPF. For the BBD and the OASPL, the absolute differences are within the measurement uncertainty. Similar results are obtained for the highest RPM, with a larger difference between C-SH samples at the BPF. The latter can be attributed to the performance variations between samples, as noise at the BPF is primarily influenced by the thickness and mean loading noise [56]. Given the small relative differences, in the following analysis, the C-SH and C-SM samples are used to compare with the straight edge case.

Table 2
Blade Passing Frequency BPF, Broadband (BBD) and Overall Sound Pressure Level (OASPL) absolute differences between propeller samples of the same geometry at the tested RPM.

	BPF (dB)		BBD (dB)		OASPL (dB)	
Absolute diff.	Sharp	Smooth	Sharp	Smooth	Sharp	Smooth
4000 RPM	1.52	1.15	0.52	0.32	0.17	0.33
8000 RPM	2.69	0.57	0.66	0.18	0.16	0.09

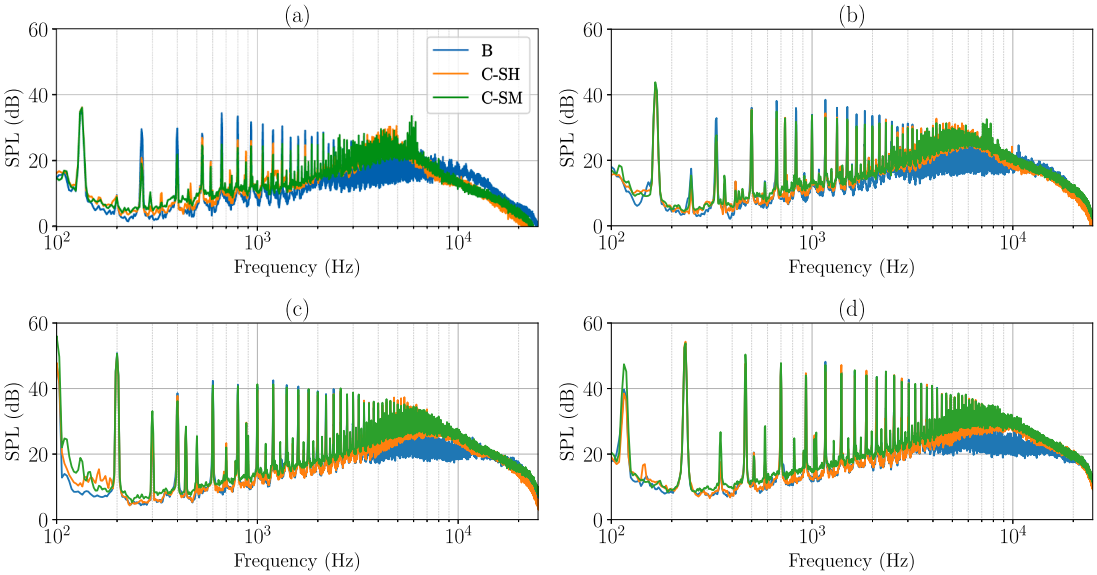

Fig. 18. SPL at 60° from the rotor plane for straight edge propeller(B) and cut-in sharp (C-SH) and smooth (C-SM) serrations for (a) 4000 RPM; (b) 5000 RPM, (c) 6000 RPM; and (d) 7000 RPM.

The spectra at 60° from the rotor plane at four rotational speeds between 4000 and 7000 RPM are shown in Fig. 18 for the straight edge, and sharp and smooth serrated propellers. Overall, the broadband noise levels are increased for both serration designs compared to the baseline. Only at high frequencies can both the sharp and smooth serrations reduce broadband noise levels, and the frequency at which they do so depends on the RPM, which is in good agreement with the findings from Pang et al. [72]. Additionally, the serrated rotors radiate less than the baseline case at the BPF harmonics at lower speeds.

Noise increase due to cut-in serrations in airfoils was measured by Chong et al. [11] and ascribed to vortex-shedding noise emanating from the serration root. Given the three-dimensionality and substantial bluntness ($t/c = 5\%$) of the serrations for the cut-in cases, the filtered spectra of the propellers are analyzed next to confirm if the noise increase is indeed due to vortex-shedding. Fig. 19(a) shows the extracted broadband signal for the straight, cut-in sharp, and cut-in smooth propellers with varying RPM. An arbitrary offset between each curve has been added for better visualization. The humps are visible for the two serration designs (smooth and sharp) with minor difference in the peak location. Their peak frequencies increase with RPM. The Strouhal number ($St = f_{peak}\, t/V_\infty$) is computed from the peak frequencies, the serration root thickness t, and the blade speed at 75% of the span and plotted as a function of the Reynolds number and RPM, as shown in Fig. 19(b).

The scaling reveals two different behaviors for each serration type. In the case of sharp serrations, the values are in the neighborhood of $St = 0.12$ with a slight tendency to increase with Reynolds number, whereas the smooth serrations do not have a discernible trend. The behavior in the latter case is attributed to the more complicated geometry of the smooth teeth as the current rotor scale could not fully alleviate the sharp or blunt edges as in the previous CD airfoil [52,60]. Note that for the sharp serrations, the St values are in fair agreement with the values reported by Chong et al. [11] for airfoils, with the caveat that their serrations were sharper (i.e. smaller serration wavelength) and the lowest tested Reynolds number was 200 000. Therefore, the cut-in serrations increase noise is mainly caused by vortex-shedding phenomena.

Moreover, the results in Fig. 19(a) suggest that at low RPMs, the cut-in serrations can eliminate the laminar boundary-layer instability tones. This serration effect is in good agreement with the experimental and numerical results by Chong et al. [11], Moreau et al. [73] and Gelot and Kim [74] on an airfoil. In the latter study, the authors suggested that the serrations weaken the aeroacoustic feedback loop at the source via two mechanisms: first, a reduction of the wall-pressure fluctuations close to the trailing edge, and second, an early breakdown of the spanwise coherence.

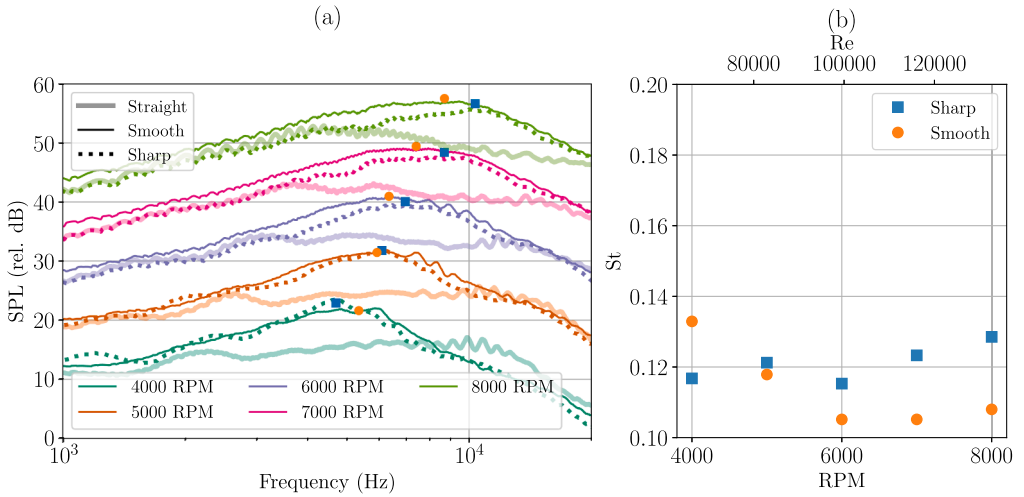

Fig. 19. Filtered spectra for straight, cut-in sharp and cut-in smooth propellers at different RPMs (with arbitrary SPL offset) (a). Strouhal number for the peak frequency as a function of Reynolds number (b).

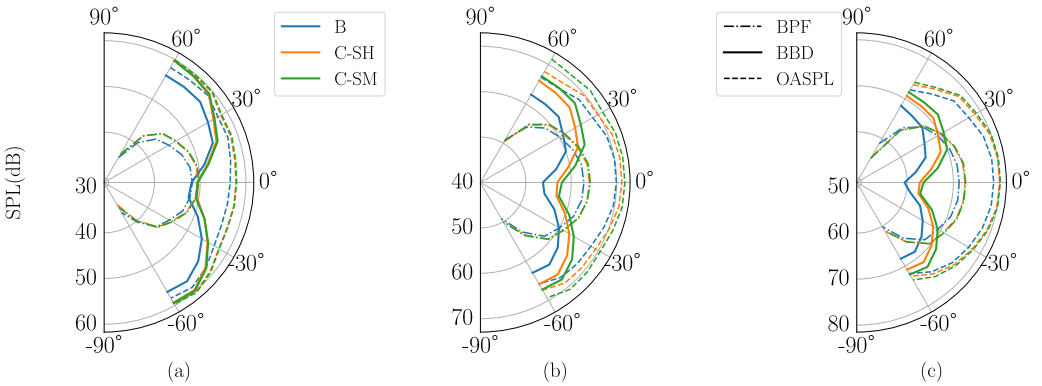

Fig. 20. BPF, Broadband and OASPL directivity for straight edge (B), sharp (C-SH) and smooth (C-SM) cut-in serrations at (a) 4000 RPM; (b) 6000 RPM and (c) 8000 RPM.

Directivity patterns for the BPF, BBD and OASPL are shown in Fig. 20 for the same geometries. The same trend as above is seen for all angular positions: an overall increase of the broadband noise component at all speeds, with the sharp teeth propeller radiating less than the smooth teeth one. At the BPF, the serrated propellers produce similar noise levels, whereas the baseline propeller radiates less across all rotational speeds. From the OASPL plots, it is noted that the broadband contribution outweighs the BPF contribution at low RPMs, particularly at higher elevation angles, whereas the opposite is true as the RPM increases.

6.2. *Add-on serrations*

The add-on serrations required a significant modification of the airfoil profile by adding the flat plate at the trailing edge with sufficient thickness to be 3D printed. Therefore, it is necessary to consider the aerodynamic and acoustic effects of the plate itself. Fig. 21 shows the thrust coefficient and figure of merit for the baseline (B), the baseline with flat plate appendix (BP), and the add-on serrations (A-ST). The discontinuity in the profile shape tangent at the rear of the airfoil results in a reduction of aerodynamic performance, as seen by a lower figure of merit at all RPMs. Since the serrated plate has less surface area than the original flat plate appendix, the figure of merit is slightly improved for the serrated propeller (A-ST) compared to the flat plate add-on (BP), while the thrust coefficient is unchanged.

The acoustic effects of the add-on plate and serrations are shown in Fig. 22 for an observer at 60° from the rotor plane and at different RPMs. The presence of the flat plate alone reduces broadband noise below 10 kHz at all RPM and seems to be more effective than the serrated propeller for most frequencies of interest, albeit with some significant noise increase at very high frequencies. The reason behind the good acoustic performance of the propeller with the add-on plate could be attributed to an improved pressure recovery along the suction side, thanks to the add-on flat plate. The adverse pressure gradient indeed has a strong influence on the wall-pressure spectra, hence resulting in the observed beneficial acoustic effect. The frequency range at which the serrations are effective depends on the RPM, as it did for the cut-in serrations. Additionally, the propeller with the add-on serrations (A-ST)

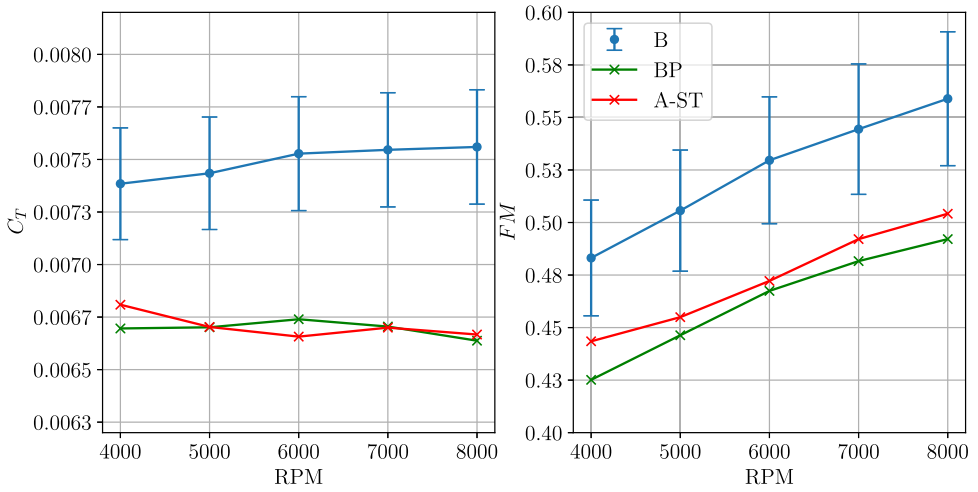

Fig. 21. (a) Thrust coefficient and (b) Figure of Merit for propellers with a straight edge (B), add-on flat plate (BP), and add-on serrations (A-ST).

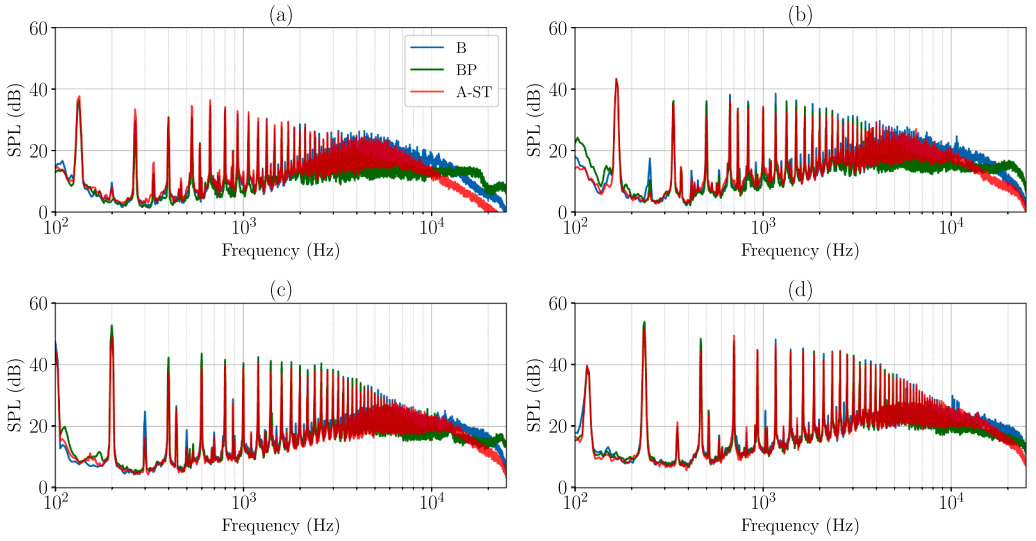

Fig. 22. SPL at 60° from the rotor plane for propellers with a straight edge(B), add-on flat plate (BP), and add-on serrations (A-ST) for (a) 4000 RPM; (b) 5000 RPM; (c) 6000 RPM; and (d) 7000 RPM.

eliminates the noise caused by the laminar boundary layer instabilities on the baseline (B), again in agreement with the airfoil results [11,73,74].

The BPF directivity is shown in Fig. 23 for the same propellers. It is noted that the propeller with the add-on plate, radiates less at positions below the rotor plane for the 4000 and 6000 RPM cases. The serrated propeller increases the BPF noise by a small amount at certain angles for some RPM and vice versa, without any discernible trend.

Both the propeller with the add-on plate and the add-on serrations reduce broadband noise at low RPMs as shown in Fig. 23. The reduction is larger at higher elevation angles and decreases with increasing RPM.

Unlike cut-in designs, the add-on design with the same serration amplitude and wavelength provides a reduction in broadband noise. Therefore, how the serrations are manufactured is crucial and must be assessed during the design phase.

6.3. Effects of forced transition and serrations

This section presents the effects of adding tripping cylinders to the propeller with add-on serrations. Starting with the aerodynamics in Fig. 24, it is noticed that the propeller with the add-on flat plate and the trip (BP-T) generates more thrust at all RPMs, while the values for the rest of the propellers tend to collapse at higher RPMs.

For the Figure of Merit, the tripped propeller with the add-on serrations (A-ST-T) has the worst performance. The tripped propeller (BP-T) outperforms the rest for RPMs below 6000 after which the add-on serrated propeller (A-ST) attains higher values.

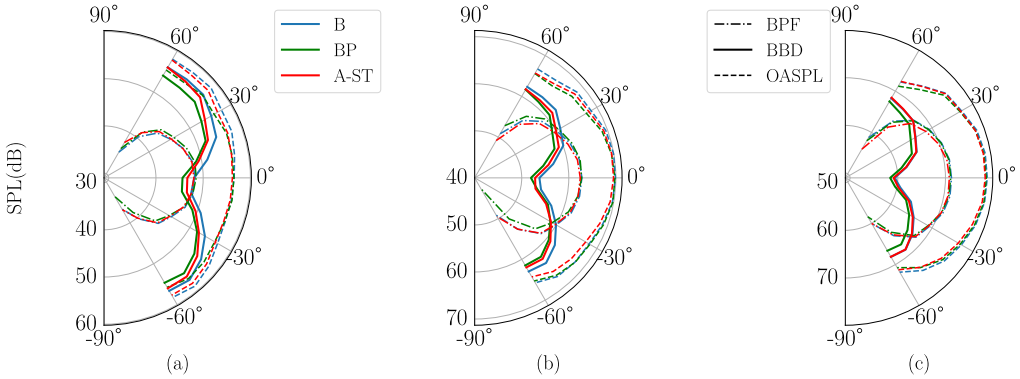

Fig. 23. BPF, Broadband, and OASPL directivity for propellers with a straight edge(B), add-on flat plate(BP), and add-on serrations(A-ST) for (a) 4000 RPM; (b) 6000 RPM, and (c) 8000 RPM.

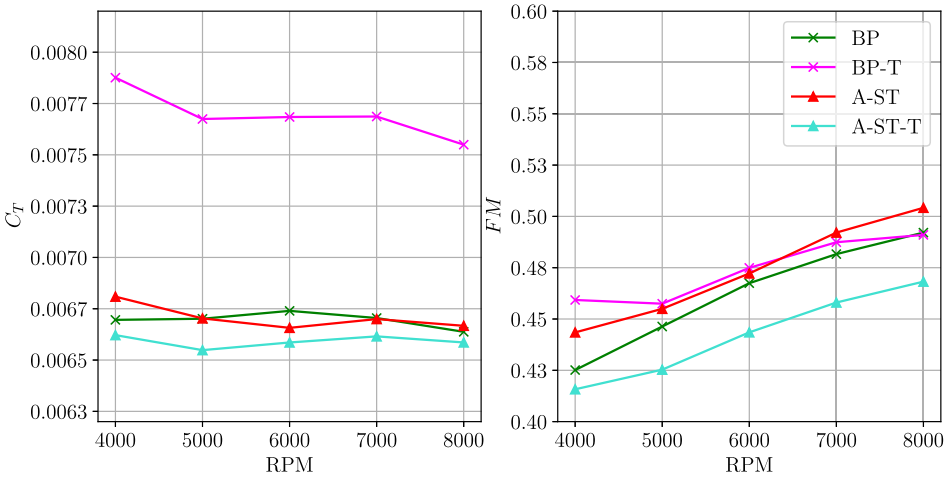

Fig. 24. (a) Thrust coefficient and (b) Figure of Merit for clean and tripped propellers with an add-on plate (BP, BP-T) and add-on serrations (A-ST, A-ST-T).

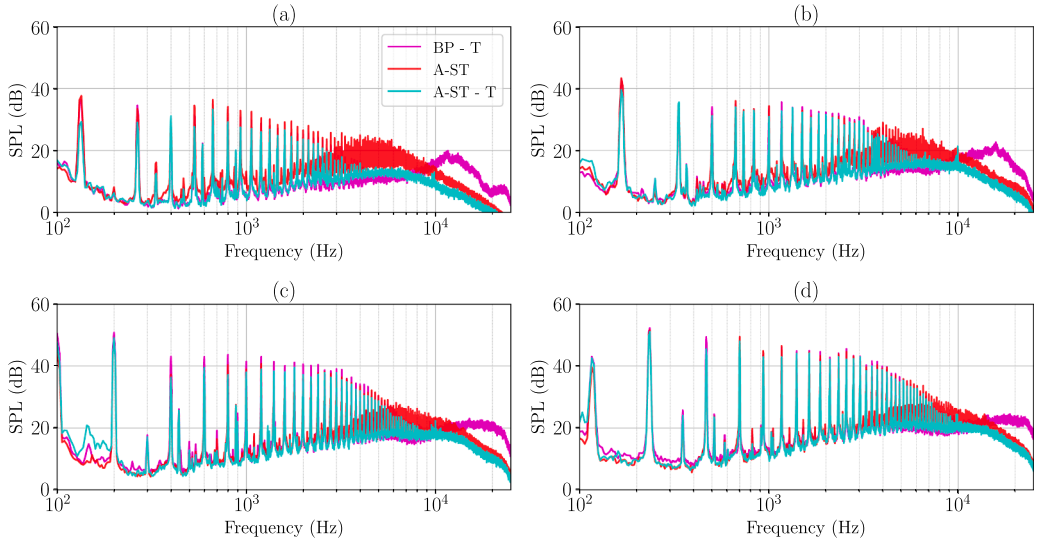

Fig. 25. SPL at 60° from the rotor plane for clean and tripped propellers with add-on serrations (A-ST, A-ST-T) and for the tripped propeller with add-on flat plate (BP-T) at (a) 4000 RPM, (b) 5000 RPM, (c) 6000 RPM, and (d) 7000 RPM.

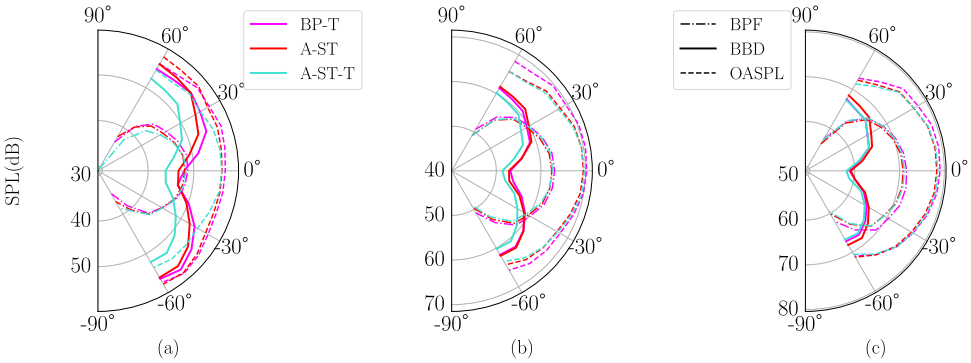

Fig. 26. BPF, broadband, and OASPL directivity for clean and tripped propellers with add-on serrations (A-ST, A-ST-T) and for the tripped propeller with add-on flat plate (BP-T) at (a) 4000 RPM, (b) 6000 RPM, and (c) 8000 RPM.

Table 3
BPF, BBD, OASPL noise reductions, and FM and C_T relative differences for all tested propellers with respect to their corresponding baselines at 4000 RPM.

	Reference	BPF(dB)	BBD(dB)	OASPL(dB)	% FM	% C_T
C-SH	B	−0.9	−2.1	−2.0	+0.9	+4.6
C-SM	B	−0.8	−2.2	−1.9	−6.5	+1.4
A-ST	BP	−1.5	−1.1	−2.5	+4.3	+1.7
A-ST-T	BP-T	+7.0	+4.2	+1.6	−9.5	−16

Table 4
BPF, BBD, OASPL noise reductions, and FM and C_T relative differences for all tested propellers with respect to their corresponding baselines at 6000 RPM.

	Reference	BPF(dB)	BBD(dB)	OASPL(dB)	% FM	% C_T
C-SH	B	+0.5	−3.2	−1.5	−5.0	+0.9
C-SM	B	+0.2	−4.6	−4.7	−9.0	−0.9
A-ST	BP	+3.7	−1.0	−0.1	+1.0	−1.2
A-ST-T	BP-T	+1.7	+1.7	+2.5	−6.6	−14

Table 5
BPF, BBD, OASPL noise reductions, and FM and C_T relative differences for all tested propellers with respect to their corresponding baselines at 8000 RPM.

	Reference	BPF(dB)	BBD(dB)	OASPL(dB)	% FM	% C_T
C-SH	B	+3.4	−3.6	−1.3	−6.2	−0.2
C-SM	B	+3.8	−5.2	−1.9	−8.0	−0.5
A-ST	BP	+2.0	−2.1	−1.1	+2.5	+0.4
A-ST-T	BP-T	+0.3	+0.6	+1.4	−4.6	−13

The spectra in Fig. 25 show that the compound effect of the trip and the serrations (A-ST-T) results in noise reductions over the whole frequency range at all RPMs, noting that the tripped propeller with the add-on plate (BP-T) slightly outperforms the rest in the low-frequency range. Note that the humps beyond 10 kHz in the add-on tripped case are not present in either of the serrated cases, suggesting that the serrations eliminate the LSB as mentioned in the previous section.

The propeller with add-on serrations and forced transition (A-ST-T) also outperforms the rest in terms of radiated tonal noise as shown in Fig. 26 and consistently reduces noise over the frequency range of interest, particularly at high elevation angles.

To conclude this section on experimental results, Tables 3–5 quantify the acoustic and aerodynamic trade-off due to the serrations at 4000, 6000, and 8000 RPM, respectively. For the acoustics, the BPF, BBD, and OASPL noise reductions, $\Delta SPL = SPL_{\text{reference}} - SPL_{\text{serrated}}$, for an observer at 60° from the rotor plane are shown. In contrast, the FM and C_T relative differences are used for the aerodynamics. The corresponding reference propeller is added for clarity. Note that in all cases, a positive value indicates noise reduction or an FM increase, whereas negative values indicate noise increase or FM reduction. The following conclusions can be drawn from the results. Firstly, only the add-on tripped serrations (A-ST-T) case reduces the BPF, BBD, and OASPL noise over the entire operational range tested, albeit with an associated aerodynamic penalty. A reduction of up to 9.5% in the Figure of Merit is noted at 4000 RPM, accompanied by a 4 dB decrease in broadband noise. At higher RPMs, the aerodynamic penalty is less severe with corresponding lower noise reduction benefits. For the other propellers, an FM reduction is observed at all RPMs, with a negligible thrust penalty. Noise reductions at unequal thrust levels must be interpreted with appropriate caution. To provide some

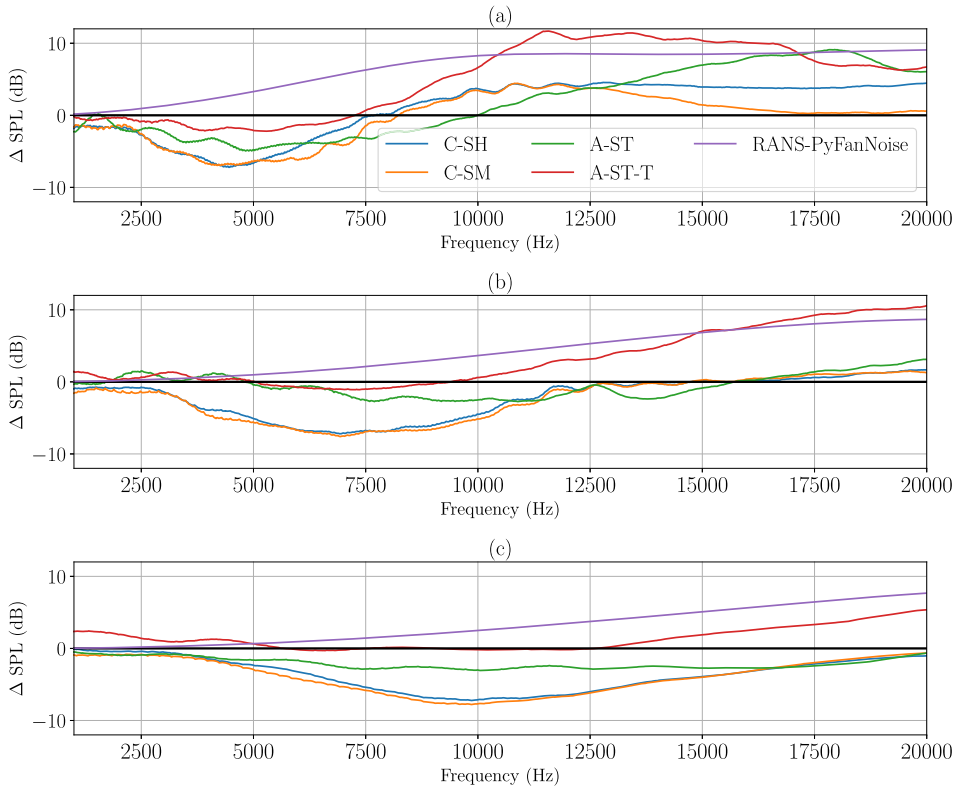

Fig. 27. Broadband noise reductions for serrated propellers and comparison with analytical predictions (a) 4000 RPM, (b) 6000 RPM, and (c) 8000 RPM.

perspective on the aerodynamic penalty, it is worth emphasizing the relatively large aerodynamic uncertainty values of up to 5%, for the FM, estimated for the baseline geometry (Fig. 15). In line with the aerodynamic penalty, a BPF noise reduction, associated with the reduction of the propeller mean loading, is observed for all the serrated geometries at high RPM. Such results confirm other studies [15,16].

6.4. Comparison with semi-analytical predictions

The noise reductions from the different propellers are compared with results obtained in the in-house code PyFanNoise with the RANS-based semi-analytical method presented in Section 2.1. Note that each serration type was compared with its respective baseline, as shown in the previous tables. Thus, the cut-in serrations (C-SH, C-SM) were compared with the Baseline (B) and the add-on serrations (A-ST, A-ST-T) with the baseline with the add-on plate (BP, BPT) in clean and tripped configurations. Fig. 27 shows the broadband noise level reductions, ΔSPL, from the different serrated propellers and compares them with the theoretical predictions for an observer at 60° from the rotor plane. The frequency range used to calculate the difference is between 1 and 20 kHz.

At 4000 RPM, all the serrated propellers increase broadband noise, for frequencies below around 7 kHz. Beyond 7 kHz, the propellers with trip add-on serrations and the sharp serrations reduce broadband noise. At this RPM, there are significant differences between the cut-in sharp and smooth cases, with the latter yielding lower reductions beyond 12 kHz. Note that the differences between sharp and smooth serrations are less noticeable with increasing RPM. Notably, the add-on trip and the sharp case yield similar noise reduction trends past 10 kHz. At this RPM, the add-on tripped case provides more than 10 dB of noise reduction, particularly close to 10 kHz. Note that the effectiveness of serrations at low RPM is in line with findings from other studies [14,16].

For the 6000 RPM case, the frequency range at which noise reductions occur shifts to higher frequencies, with the add-on (clean) and cut-in cases decreasing noise only past 16 kHz. The add-on tripped case shows around 1 dB noise increase below 10 kHz and yields noise reductions up to 10 dB beyond this frequency.

At the highest RPM, only the add-on tripped serrations reduces noise, being effective below 5 kHz and beyond 12.5 kHz. The cut-in cases perform almost equally, yielding a 7 dB noise increase at 10 kHz, and a lower noise increase at other frequencies. There are a few takeaways regarding the theoretical predictions based on the extended Ayton's model, given that its assumptions (infinite flat plate, fully turbulent flow) mainly correspond to the A-ST-T case only. First, the model cannot predict any noise increase since this is related to vortex shedding for cut-in serrations and, likely, to secondary flow effects for add-on ones [10]. Secondly, the model over-predicts the maximum noise reduction at all RPMs by 4-5 dB. Thirdly, the model captures the trend of decreasing serration

benefit with increasing RPM for the add-on tripped case, meeting the model assumptions more closely. Lastly, it predicts the spectral shape of the noise reduction and the location of the maximum noise reductions, roughly 12, 17.5, and 20 kHz for 4000, 6000, and 8000 RPM, respectively. Thus, the models and methodology presented may be used during the early propeller design, particularly at low RPM, to get an insight into the frequency range and theoretical noise reductions. Due to the inherent assumptions of the tested model for serrations, it is important to recall that only trends can be captured. Transitional boundary layers on a rotating blade and the manufacturing details of the serration installation along the propeller edge may only be captured with more advanced hybrid CAA methods [31,32,57]. Yet, to reach accurate noise predictions, such methods must be able to account for the proper turbulence excitation mechanism of complex three-dimensional transitioning flow and the precise scattering of the fluctuations by the actual geometry.

7. Conclusions and further work

The study has assessed theoretical noise reductions using serrations for a representative UAV propeller in hover. The serration design had accounted for manufacturing constraints such as minimum thickness. Different propellers based on a NACA 0012 airfoil section with add-on, cut-in sharp, and cut-in smooth serrations have been built with SLA rapid prototyping. Two baselines corresponding to the original propeller and a modified one with an add-on flat plate have been manufactured for better comparison. The spectra of the original rotor show equidistant narrow-band humps at almost all tested rotational speeds. These tones correspond to laminar boundary-layer instability noise on the blade suction sides, matching previous experiments on the NACA 0012 airfoil. Additional prototypes with tripping elements at 10% from the leading edge have been manufactured to study the impact of forced transition on the baselines and add-on serrated propellers. As previously found on airfoils, tripping alleviates the laminar boundary-layer instability noise.

This work demonstrates that with SLA it is possible to obtain similar samples for the cut-in serrations, for which small deviations have been found, particularly for the propeller with smooth teeth. The present study stresses the importance of considering how serrations are installed in the design. The propellers with cut-in serrations exhibit noise reductions for different frequencies at different RPMs, but noise increases below those frequency ranges. Some of the noise increase is attributed to vortex shedding characterized by a Strouhal number based on the serration root thickness and the relative velocity at 75% span of 0.12, very close to what was previously found on airfoils. The tripped propeller with the add-on serrations is the most effective at reducing broadband noise with an aerodynamic penalty of up to 9.5% in the Figure of Merit.

The theoretical model, the assumptions of which are close to the tripped propeller with add-on serrations (A-ST-T), correctly predicts the noise reduction frequency range for this case. Additionally, the analytical results capture the noise reduction decrease with increasing RPM trend. However, the predictions for cut-in serrations do not agree with the experimental data, as these serrations deviate significantly from the idealized one. The experimental results show that both cut-in and add-on serrations are valid methods to reduce TEN at high frequencies. However, in both cases, the serrations are most effective at low RPMs, where broadband noise dominates the spectra. Additionally, reductions of up to 3 dB have been observed at the BFP at high RPMs. Overall, although the noise reductions are over-predicted for up to 5 dB, the low-order method can provide initial guidelines for serration design. Future studies will include more recent serration models that can provide fast and reliable estimates for noise reductions. Limitations of acoustic models as well as the aerodynamic penalties incurred by constraints in the serrations manufacturing could be investigated using high fidelity simulations [2,31,57,75,76]. This study may also serve as a stepping stone for further validation of computational aeroacoustic methods [4,32,77], particularly those aimed at optimizing serrated propeller designs. To this end, the experimental database is made publicly available [78].

CRediT authorship contribution statement

Jorge Santamaria: Writing – review & editing, Writing – original draft, Visualization, Validation, Methodology, Formal analysis, Data curation, Conceptualization; **Sylvain Belliot:** Investigation, Visualization; **Marlène Sanjosé:** Writing – review & editing, Visualization, Supervision, Software, Methodology, Funding acquisition, Formal analysis, Conceptualization; **Romain Gojon:** Writing – review & editing, Resources, Investigation, Formal analysis; **Stéphane Moreau:** Writing – review & editing, Supervision, Methodology.

Data availability

Experimental results are made open-acces on https://doi.org/10.57745/L8MNF5.

Declaration of competing interest

The authors declare no conflict of interest. The present work has been enabled by the following research funding:

– FRQNT Projet de Recherche en Équipe FRQNT-PR-300387.
– NSERC Discovery Grant RGPIN-2020-05919.

Acknowledgments

The authors acknowledge the partners of the UHEQ Consortium II and III at Université de Sherbrooke, which develops and provides the acoustic software PyFanNoise for this research.

Appendix A. Effective angle of attack extraction from RANS simulations

In order to obtain an estimate of the effective angle of attack and thus identify zones of tonal emission in Fig. 9, the RANS results from Santamaria et al. [41] are used. The first step in the calculation is to perform a meridional average of the flow through the propeller. Secondly, a line at a distance of 10% chord upstream of the propeller is chosen for the extraction of the velocities in the relative reference frame. The upstream velocity triangle then provides the angle δ as shown in Fig. A.28(a). Since the blade pitch β is constant along the span, the effective angle of attack, α_{eff}, is easily calculated.

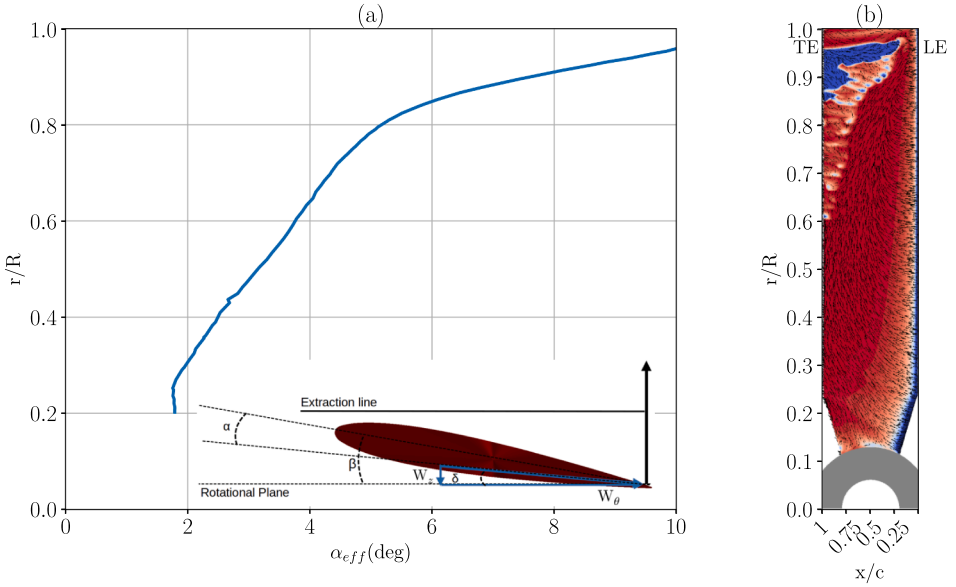

Fig. A.28. Effective angle of attack along the span. Miniature shows velocity triangle (a). Wall-shear stress streaklines imposed over contours of turbulence intermittency at 6000 RPM. Blue regions indicate turbulent flow, whereas red marks laminar flow (b). (For interpretation of the references to colour in this figure legend, the reader is referred to the web version of this article).

The regions of transitional flow along the span are identified with the intermittency contours in Fig. A.28(b). For r/R below 0.6, the boundary layer remains laminar, the region between 0.6 and 0.8 shows transitional flow, and the outermost part of the blade is fully-turbulent. Therefore, the possible zones where the instabilities in the boundary occur correspond to the region between 0.6 and 0.8. In this region, the effective angle of attack is between 3.5° and 5°, which correspond to zones of laminar boundary layer instability tones from the suction side.

Appendix B. Laminar boundary layer instability tones sensitivity to manufacturing

Laminar boundary layer instability tones were identified in the baseline propeller in Section 5.1. To show the reproducibility of this phenomenon, the data set from three identically designed rotors in Gojon et al. [56] will be used. The propellers materials, manufacturing details, and assembly method are summarized in Table B.6. In the present study, the propeller was printed as a single piece, whereas the blades and hub were individually printed and assembled for the other propellers.

Table B.6
Propeller materials and manufacturing details.

Propeller	Material	Printing direction	Assembly
JASA 1	Rigid resin	1	3 pieces
JASA 2	Rigid resin	2	3 pieces
JASA 3	Grey resin	1	3 pieces
Present study	Rigid resin	NA	1 piece

Using the same filtering techniques described in Section 5.1 the filtered spectra and identified tones for the JASA propellers and the baseline propeller of the present study are shown in Fig. B.29 where the SPL of each propeller has been arbitrarily shifted

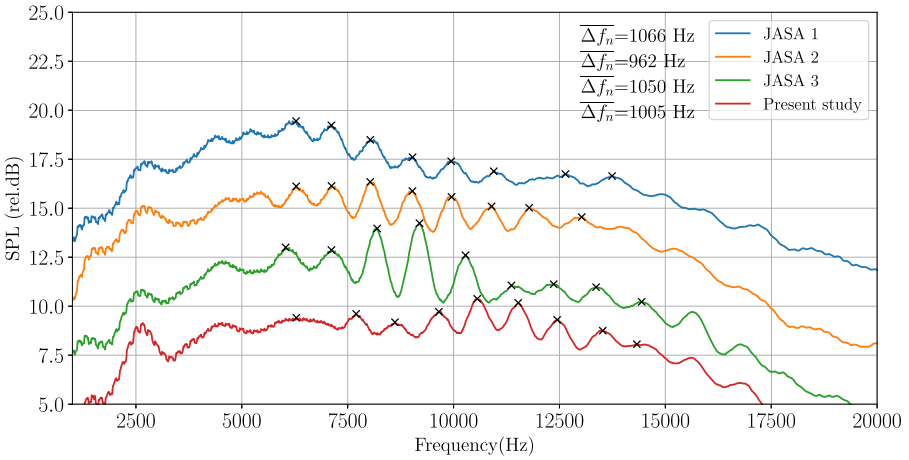

Fig. B.29. Filtered spectra for identically designed 2-bladed rotors with laminar boundary layer tones identified at 5000 RPM and for an observer at 60 °.

to avoid cluttering. While all the propellers display peaks, their prominences differ. For example, the JASA-3 propeller peaks are well-defined, with an easily identifiable central peak. In contrast, the peaks from the JASA-1 propeller are of lower amplitude. Additionally, the peaks for all the JASA propellers are identified at similar frequencies, while the present study propeller peaks occur at higher frequencies. Despite the frequencies not matching, the average peak separation of all identified peaks is on the same order of magnitude. Lastly, note that the hump peak shifts from propeller to propeller. Given that the geometry is identical, this can be mostly attributed to material, printing, and assembly methods, all of which can directly impact the blade surface finish and thus the evolution of the transitional regions along the blade.

References

[1] D. Casalino, E. Grande, G. Romani, D. Ragni, F. Avallone, Definition of a benchmark for low Reynolds number propeller aeroacoustics, Aerosp. Sci. Technol. 113 (2021) 106707. https://doi.org/10.1016/j.ast.2021.106707
[2] C. Thurman, D.D.J. Boyd, P. Buning, G. Reboul, C. Benoit, NASA/ONERA Collaboration on small hovering rotor broadband noise prediction using lattice-Boltzmann method and structured Navier-Stokes solvers, in: 30th AIAA/CEAS Aeroacoustics Conference, American Institute of Aeronautics and Astronautics, 2024, p. 2024. https://doi.org/10.2514/6.2024-3106
[3] J. Yin, K.-S. Rossignol, L. Rottmann, T. Schwarz, Numerical studies on small rotor configurations with validation using acoustic wind tunnel data, CEAS Aeronaut. J. 15 (2024) 671–702. https://doi.org/10.1007/s13272-023-00671-0
[4] J. Yin, F.D. Gregorio, K.-S. Rossignol, L. Rottmann, G. Ceglia, G. Reboul, G. Barakos, G. Qiao, M. Muth, M. Kessler, A. Visingardi, M. Barbarino, F. Petrosino, A. Zanotti, N. Oberti, A. Savino, G. Bernardini, C. Poggi, L. Abergo, F. Caccia, A. Guardone, C. Testa, S. Zaghi, Acoustic and aerodynamic evaluation of DLR small-scale rotor configurations within GARTEUR AG26, CEAS Aeronaut. J. 16 (2025) 1175–1196. https://doi.org/10.1007/s13272-024-00790-2
[5] N.S. Zawodny, D.D. Boyd, C.L. Burley, Acoustic characterization and prediction of representative, small-scale rotary-wing unmanned aircraft system components, in: VFS International Powered Lift Conference, West Palm Beach, FL, 2016.
[6] C. Thurman, N. Zawodny, J. Baeder, Computational Prediction of Broadband Noise from a Representative Small Unmanned Aerial System Rotor, VFS, 2020.
[7] N.A. Pettingill, N.S. Zawodny, C.S. Thurman, L.V. Lopes, Acoustic and performance characteristics of an ideally twisted rotor in hover, in: AIAA SCITECH 2021 FORUM, 2021.
[8] S.A.S. Ali, M. Azarpeyvand, C.R. I.D. Silva, Trailing-edge flow and noise control using porous treatments, J. Fluid Mech. 850 (2018) 83–119. https://doi.org/10.1017/jfm.2018.430
[9] T. Geyer, E. Sarradj, C. Fritzsche, Measurement of the noise generation at the trailing edge of porous airfoils, Exp. Fluids 48 (2010) 291–308. https://doi.org/10.1007/s00348-009-0739-x
[10] M. Gruber, Airfoil Noise Reduction by Edge Treatments, Technical Report, University of Southampton, Institute of Sound and Vibration, 2012. Ph.D. thesis.
[11] T.P. Chong, A. Vathylakis, P.F. Joseph, M. Gruber, Self-noise produced by an airfoil with nonflat plate trailing-edge serrations, AIAA J. 51 (2013) 2665–2677. https://doi.org/10.2514/1.J052344
[12] A. Vathylakis, T.P. Chong, P.F. Joseph, Poro-serrated trailing-edge devices for airfoil self-noise reduction, AIAA J. 53 (2015) 3379–3394. https://doi.org/10.2514/1.J053983
[13] S. Lee, L. Ayton, F. Bertagnolio, S. Moreau, T.P. Chong, P. Joseph, Turbulent boundary layer trailing-edge noise: theory, computation, experiment, and application, Prog. Aerosp. Sci. 126 (2021) 100737. https://doi.org/10.1016/j.paerosci.2021.100737
[14] Z. Ning, R.W. Wlezien, H. Hu, An experimental study on small UAV propellers with serrated trailing edges, in: 14th AIAA Fluid Dynamics Conference, Denver, Colorado, American Institute of Aeronautics and Astronautics, 2017, p. 47. https://doi.org/10.2514/6.2017-3813
[15] Y. Yang, Y. Wang, Y. Liu, H. Hu, Z. Li, Noise reduction and aerodynamics of isolated multi-copter rotors with serrated trailing edges during forward flight, J. Sound Vib. 489 (2020) 115688. https://doi.org/10.1016/j.jsv.2020.115688
[16] B. Zang, L.P. Hanson, A. Stoltz, W.H. Ho, X. Liu, M. Azarpeyvand, Numerical and experimental investigation of propeller noise with trailing-edge serrations, in: AIAA AVIATION 2023 Forum, San Diego, CA and Online, American Institute of Aeronautics and Astronautics, 2023. https://doi.org/10.2514/6.2023-3835
[17] P. Candeloro, D. Ragni, T. Pagliaroli, Experimental investigation on the application of serrated trailing edge propellers for drone noise reduction, Appl. Acoust. 242 (2026) 111045. https://doi.org/10.1016/j.apacoust.2025.111045
[18] M.S. Howe, Aerodynamic noise of a serrated trailing edge, J. Fluids Struct. 5 (1991) 33–45. https://doi.org/10.1016/0889-9746(91)80010-B
[19] R.D. Sandberg, N.D. Sandham, Direct numerical simulation of turbulent flow past a trailing edge and the associated noise generation, J. Fluid Mech. 596 (2008) 353–385. https://doi.org/10.1017/S0022112007009561
[20] M. Wang, P. Moin, Computation of trailing-edge flow and noise using large-eddy simulation, AIAA J. 38 (2000) 2201–2209. https://doi.org/10.2514/2.895
[21] E. Manoha, B. Troff, P. Sagaut, Trailing-edge noise prediction using large-eddy simulation and acoustic analogy, AIAA J. 38 (2000) 575–583. https://doi.org/10.2514/2.1015

[22] J. Winkler, H. Wu, S. Moreau, T. Carolus, R.D. Sandberg, Trailing-edge broadband noise prediction of an airfoil with boundary-layer tripping, J. Sound Vib. 482 (2020) 115450. https://doi.org/10.1016/j.jsv.2020.115450
[23] M. Wang, J.B. Freund, S.K. Lele, Computational prediction of flow-generated sound, Annu. Rev. Fluid Mech. 38 (2006) 483–512. https://doi.org/10.1146/annurev.fluid.38.050304.092036
[24] W. Devenport, N. Alexander, S. Glegg, M. Wang, The sound of flow over rigid walls, Annu. Rev. Fluid Mech. 50 (2018) 435–458. https://doi.org/10.1146/annurev-fluid-122316-045056
[25] R. Ewert, W. Schröder, On the simulation of trailing edge noise with a hybrid LES/APE method, J. Sound Vib. 270 (2004) 509–524. https://doi.org/10.1016/j.jsv.2003.09.047
[26] V.B. Ananthan, R.A.D. Akkermans, Trailing edge noise reduction using bio-inspired finlets, J. Sound Vib. 549 (2023) 117553. https://doi.org/10.1016/j.jsv.2023.117553
[27] P. Bernicke, R.A.D. Akkermans, V.B. Ananthan, R. Ewert, J. Dierke, L. Rossian, A zonal noise prediction method for trailing-edge noise with a porous model, Int. J. Heat Fluid Flow 80 (2019) 108469. https://doi.org/10.1016/j.ijheatfluidflow.2019.108469
[28] A. Bissuel, G. Allaire, L. Daumas, S. Barré, F. Rey, Linearized Navier-Stokes equations for aeroacoustics using stabilized finite elements: boundary conditions and industrial application to aft-fan noise propagation, Comput. Fluids 166 (2018) 32–45. https://doi.org/10.1016/j.compfluid.2018.01.011
[29] G. Gabard, H. Bériot, A.G. Prinn, K. Kucukcoskun, Adaptive, high-order finite-element method for convected acoustics, AIAA J. 56 (2018) 3179–3191. https://doi.org/10.2514/1.J057054
[30] S.M.A. Moghadam, M. Meinke, W. Schröder, Numerical analysis of the acoustic field of a ducted axial fan at varying tip clearances, Acta Acust. United Acust. 105 (2019) 43–55. https://doi.org/10.3813/AAA.919286
[31] G. Romani, E. Grande, F. Avallone, D. Ragni, D. Casalino, Performance and noise prediction of low-Reynolds number propellers using the Lattice-Boltzmann method, Aerosp. Sci. Technol. 125 (2022) 107086. https://doi.org/10.1016/j.ast.2021.107086
[32] R. Ewert, J. Dierke, J. Siebert, A. Neifeld, C. Appel, M. Siefert, O. Kornow, CAA broadband noise prediction for aeroacoustic design, J. Sound Vib. 330 (2011) 4139–4160. https://doi.org/10.1016/j.jsv.2011.04.014
[33] Y.C. Küçükosman, J. Christophe, C. Schram, Trailing edge noise prediction based on wall pressure spectrum models for NACA0012 airfoil, J. Wind Eng. Ind. Aerodyn. 175 (2018) 305–316. https://doi.org/10.1016/j.jweia.2018.01.030
[34] M.S. Howe, A review of the theory of trailing edge noise, J. Sound Vib. 61 (1978) 437–465. https://doi.org/10.1016/0022-460X(78)90391-7
[35] R. Schlinker, R. Amiet, Helicopter rotor trailing edge noise, in: 7th Aeroacoustics Conference, Palo Alto,CA, U. S. A., American Institute of Aeronautics and Astronautics, 1981. https://doi.org/10.2514/6.1981-2001
[36] N. Hu, N. Reiche, R. Ewert, Simulation of turbulent boundary layer wall pressure fluctuations via Poisson equationand synthetic turbulence, J. Fluid Mech. 826 (2017) 421–454. https://doi.org/10.1017/jfm.2017.448
[37] F. Bertagnolio, A. Fischer, C. Appel, M. Herr, F. Seel, T. Lutz, K. Boorsma, G. Schepers, M. Botero, D. Casalino, W.V.D. Velden, C. Sucameli, P. Bortolotti, Wind turbine noise code benchmark: a comparison and verification exercise, in: 10th International Conference on Wind Turbine Noise, Dublin, 2023.
[38] S. Lee, Empirical wall-pressure spectral modeling for zero and adverse pressure gradient flows, AIAA J. 56 (2018) 1818–1829. https://doi.org/10.2514/1.J056528
[39] M. Sanjosé, S. Moreau, Fast and accurate analytical modeling of broadband noise for a low-speed fan, J. Acoust. Soc. Am. 143 (2018) 3103–3113. https://doi.org/10.1121/1.5038265
[40] D. Lallier-Daniels, F. Bolduc-Teasdale, S. Moreau, P. Guilleminot-Simon, M. Lévesque-Leduc, D. Rancourt, M. Sanjosé, Predictive acoustic modeling of open propellers using analytical tools and RANS simulations, in: VFS International Powered Lift Conference, San Jose, CA, USA, Vertical Flight Society, 2020, pp. 66–77.
[41] J. Santamaria, A. Bierrenbach-Lima, M. Sanjosé, S. Moreau, Shape considerations for the design of propellers with trailing edge serrations, J. Sound Vib. 595 (2025) 118771. https://doi.org/10.1016/j.jsv.2024.118771
[42] J.E.F. Williams, L.H. Hall, Aerodynamic sound generation by turbulent flow in the vicinity of a scattering half plane, J. Fluid Mech. 40 (1970) 657. https://doi.org/10.1017/S0022112070000368
[43] R.K. Amiet, Noise due to turbulent flow past a trailing edge, J. Sound Vib. 47 (1976) 387–393. https://doi.org/10.1016/0022-460X(76)90948-2
[44] R.K. Amiet, Noise Produced by Turbulent Flow Into a Rotor: Theory Manual for Noise Calculation, National Aeronautics and Space Administration, Langley Research Center, 1989.
[45] B. Lyu, M. Azarpeyvand, S. Sinayoko, Prediction of noise from serrated trailing edges, J. Fluid Mech. 793 (2016) 556–588. https://doi.org/10.1017/jfm.2016.132
[46] H. Akila, B.G. Marinus, S. Larbi, Trailing edge noise of innovative mini-RPA propeller blade geometry, in: AIAA/CEAS Aeroacoustics Conference, American Institute of Aeronautics and Astronautics, 2018. https://doi.org/10.2514/6.2018-3451
[47] L.J. Ayton, Analytic solution for aerodynamic noise generated by plates with spanwise-varying trailing edges, J. Fluid Mech. 849 (2018) 448–466. https://doi.org/10.1017/jfm.2018.431
[48] B. Lyu, L.J. Ayton, Rapid noise prediction models for serrated leading and trailing edges, J. Sound Vib. 469 (2020) 115136. https://doi.org/10.1016/j.jsv.2019.115136
[49] S.K. Li, S. Lee, Extensions and applications of Lyu and Ayton's serrated trailing-edge noise model to rotorcraft, in: 28th AIAA/CEAS Aeroacoustics 2022 Conference, Southampton, UK, American Institute of Aeronautics and Astronautics, 2022. https://doi.org/10.2514/6.2022-2916
[50] S. Sinayoko, M. Kingan, A. Agarwal, Trailing edge noise theory for rotating blades in uniform flow, Proc. R. Soc. A Math. Phys. Eng. Sci. 469 (2013) 20130065. https://doi.org/10.1098/rspa.2013.0065
[51] L.J. Ayton, P. Chaitanya, An analytical and experimental investigation of aerofoil-turbulence interaction noise for plates with spanwise-varying leading edges, J. Fluid Mech. 865 (2019) 137–168. https://doi.org/10.1017/jfm.2019.78
[52] S. Moreau, M. Sanjosé, B. Lyu, L.J. Ayton, Analytical, numerical and experimental investigation of trailing-edge noise reduction on a controlled diffusion airfoil with serrations, in: 25th AIAA/CEAS Aeroacoustics Conference, Delft, The Netherlands, American Institute of Aeronautics and Astronautics, 2019, p. 25. https://doi.org/10.2514/6.2019-2450
[53] H. Tian, B. Lyu, Prediction of broadband noise from rotating blade elements with serrated trailing edges, Phys. Fluids 34 (2022) 85109. https://doi.org/10.1063/5.0094423
[54] M. Roger, S. Moreau, Back-scattering correction and further extensions of Amiet's trailing-edge noise model. Part 1: theory, J. Sound Vib. 286 (2005) 477–506. https://doi.org/10.1016/j.jsv.2004.10.054
[55] A. Caiazzo, S. Pargal, H. Wu, M. Sanjosé, J. Yuan, S. Moreau, On the effect of adverse pressure gradients on wall-pressure statistics in a controlled-diffusion aerofoil turbulent boundary layer, J. Fluid Mech. 960 (2023) 17. https://doi.org/10.1017/jfm.2023.157
[56] R. Gojon, T. Jardin, H. Parisot-Dupuis, Experimental investigation of low Reynolds number rotor noise, J. Acoust. Soc. Am. 149 (2021) 3813–3829. https://doi.org/10.1121/10.0005068
[57] D.V. Shenoy, R. Gojon, T. Jardin, M.C. Jacob, Aerodynamic and acoustic study of a small scale lightly loaded hovering rotor using large eddy simulation, Aerosp. Sci. Technol. 150 (2024) 109219. https://doi.org/10.1016/j.ast.2024.109219
[58] M. Gruber, P. Joseph, T.P. Chong, Experimental investigation of airfoil self noise and turbulent wake reduction by the use of trailing edge serrations, in: 16th AIAA/CEAS Aeroacoustics Conference, Stockholm. Sweden, American Institute of Aeronautics and Astronautics, 2010. https://doi.org/10.2514/6.2010-3803
[59] P. Kholodov, S. Moreau, Optimization of trailing-edge serrations with and without slits for broadband noise reduction, J. Sound Vib. 490 (2021) 115736. https://doi.org/10.1016/j.jsv.2020.115736
[60] M. Sanjose, C. Meon, S. Moreau, A. Idier, P. Laffay, Direct numerical simulation of acoustic reduction using serrated trailing-edge on an isolated airfoil, in: 20th AIAA/CEAS Aeroacoustics Conference, Atlanta, GA, American Institute of Aeronautics and Astronautics, 2014. https://doi.org/10.2514/6.2014-2324
[61] E. Gowree, T. Jaroslawski, B. Mellot, R. Gojon, Noise reduction on low Reynolds number rotors by boundary layer transition, Applied Acoustics 210 (2023) 109446. https://doi.org/10.1016/j.apacoust.2023.109446

[62] P.L. Volsi, G. Brogna, R. Gojon, T. Jardin, H. Parisot-Dupuis, J.-M. Moschetta, Analysis of MAV rotors optimized for low noise and aerodynamic efficiency with operational constraints, Fluids 9 (2024) 96. https://doi.org/10.3390/fluids9040096
[63] N.S. Zawodny, D.D. Boyd, Investigation of rotor-airframe interaction noise associated with small-Scale rotary-wing unmanned aircraft systems, J. Am. Helicopter Soc. 65 (2020) 1–17. https://doi.org/10.4050/JAHS.65.012007
[64] A. Savitzky, M.J.E. Golay, Smoothing and differentiation of data by simplified least squares procedures, Anal. Chem. 36 (1964) 1627–1639. https://doi.org/10.1021/ac60214a047
[65] R.W. Paterson, P.G. Vogt, M.R. Fink, C.L. Munch, Vortex noise of isolated airfoils, J. Aircr. 10 (1973) 296–302. https://doi.org/10.2514/3.60229
[66] C.K.W. Tam, Discrete tones of isolated airfoils, J. Acoust. Soc. Am. 55 (1974) 1173–1177. https://doi.org/10.1121/1.1914682
[67] G. Yakhina, M. Roger, S. Moreau, L. Nguyen, V. Golubev, Experimental and analytical investigation of the tonal trailing-edge noise radiated by low Reynolds number aerofoils Acoustics 2 (2020) 293–329. https://doi.org/10.3390/acoustics2020018
[68] H. Arbey, J. Bataille, Noise generated by airfoil profiles placed in a uniform laminar flow, J. Fluid Mech. 134 (1983) 33–47. https://doi.org/10.1017/S0022112083003201
[69] S. Pröbsting, F. Scarano, S.C. Morris, Regimes of tonal noise on an airfoil at moderate Reynolds number, J. Fluid Mech. 780 (2015) 407–438. https://doi.org/10.1017/jfm.2015.475
[70] D. Vittal-Shenoy, R. Gojon, T. Jardin, M.C. Jacob, Aeroacoustic study of low Reynolds/low Mach number rotor using LES, in: 56th 3AF International Conference on Applied Aerodynamics, Tolouse, 2022.
[71] J. Rendon, S. Moreau, R. Gojon, M. Bauerheim, LBM and iLES comparison for the aaerodynamic and acoustic characteristics of a low-speed rotor, in: 30th AIAA/CEAS Aeroacoustics Conference, American Institute of Aeronautics and Astronautics, 2024, p. 2024. Aeroacoustics Conferences. https://doi.org/10.2514/6.2024-3046
[72] E. Pang, A. Cambray, D. Rezgui, M. Azarpeyvand, S.A. Showkat Ali, Investigation towards a better understanding of noise generation from UAV propellers, in: AIAA/CEAS Aeroacoustics Conference, Atlanta, Georgia, American Institute of Aeronautics and Astronautics, 2018. https://doi.org/10.2514/6.2018-3450
[73] S. Moreau, P. Laffay, A. Idier, N. Atalla, Several noise control of the trailing-edge noise of a controlled-diffusion airfoil, in: 22nd AIAA/CEAS Aeroacoustics Conference, Lyon, France, American Institute of Aeronautics and Astronautics, 2016. https://doi.org/10.2514/6.2016-2816
[74] M.B.R. Gelot, J.W. Kim, Effect of serrated trailing edges on aerofoil tonal noise, J. Fluid Mech. 904 (2020) 30. https://doi.org/10.1017/jfm.2020.724
[75] M. Jdiobe, Aeroacoustic Characterization of Coaxial Ducted Propellers/Rotors for Small UAVs, Technical Report, Oklahoma State University, United States - Oklahoma, 2024. Ph.D. thesis.
[76] J. Rendón-Arredondo, E. Vella, A.A. Ramo, M. Roger, R. Gojon, T. Jardin, S. Moreau, Aeroacoustic investigations of a rotor-beam configuration in small-size drones, J. Acoust. Soc. Am. 158 (2025) 1091–1102. https://doi.org/10.1121/10.0038975
[77] C. Polacsek, A. Cader, M. Buszyk, R. Barrier, F. Gea-Aguilera, H. Posson, Aeroacoustic design and broadband noise predictions of a fan stage with serrated outlet guide vanes, Phys. Fluids 32 (2020) 107107. https://doi.org/10.1063/5.0020190
[78] R. Gojon, J. Santamaria, M. Sanjose, S. Belliot, S. Moreau, Dataset corresponding to the publication : serration manufacturing effects on propeller trailing edge noise mechanisms, santamaria et al, 2025. https://doi.org/10.57745/L8MNF5